A poro-elastic model for triggering of production-induced earthquakes in the Groningen natural gas field by abrupt changes in well rates

T.J.W. Postma

Thesis committee:

Prof. dr. ir. J.D. Jansen (chair)
Dr. H. Hajibeygi
Dr. ir. F.C. Vossepoel
Dr. P.J. Vardon

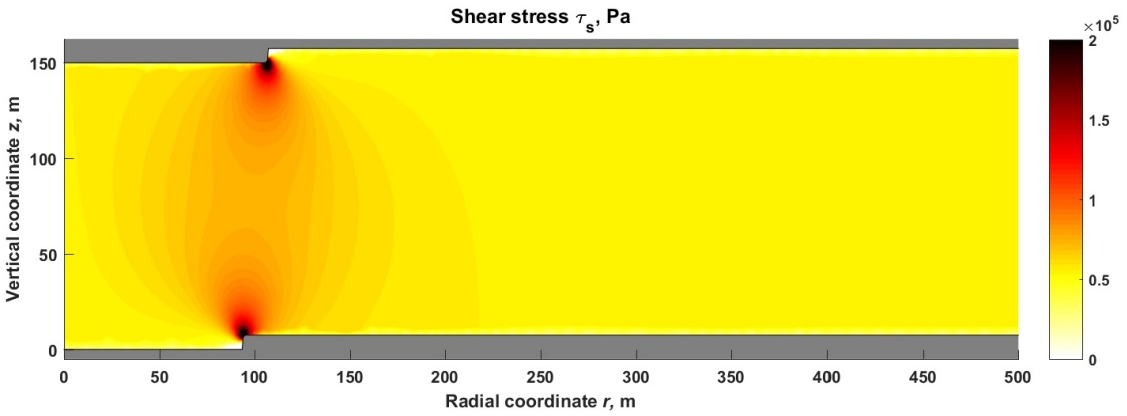

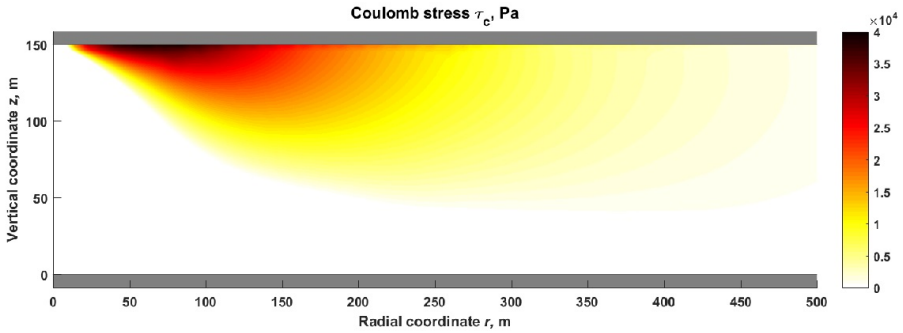

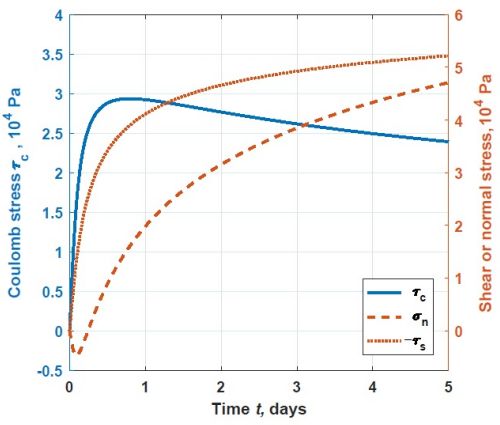

TU Delft

A poro-elastic model for triggering of production-induced earthquakes in the Groningen natural gas field by abrupt changes in well rates

by

T.J.W. Postma

to obtain the degree of Master of Science
at Delft University of Technology,
to be defended publicly on Tuesday July 18th, 2017 at 10:30 AM.

Student number:	4097688	
Project duration:	September 1st, 2016 – July 18th, 2017	
Thesis committee:	Prof. dr. ir. J.D. Jansen,	TU Delft, supervisor
	Dr. H. Hajibeygi,	TU Delft
	Dr. ir. F.C. Vossepoel,	TU Delft
	Dr. P.J. Vardon,	TU Delft

An electronic version of this thesis is available at `http://repository.tudelft.nl/`.

TU Delft

Abstract

Over the past decade, a steep increase in the number of seismic events has been observed in the Groningen gas producing region of the Northern Netherlands. It is generally accepted that these are induced by compaction of the reservoir rock due to extensive field depletion, causing a buildup of strain energy which may be released seismically when a critical stress level is reached. This study focuses not on the long term compaction, but rather on the possible triggering of fault slip by the transient flow regime surrounding a well which has undergone a sudden rate change. Assuming a unilateral decoupling between displacement and pressure, numerical experiments are conducted using a sequential finite volume-finite element solution strategy that fully incorporates second order terms in the radial flow equation. Solving for short time scales, a spatial and temporal maximum in slip-promoting stress is observed and explained physically. Although present, the transient effect is of a magnitude that raises questions about its significance, especially as the geometric irregularity of a fault with nonzero displacement causes even greater stress concentrations that grow monotonously in time.

Key Points:

- Transient maxima in slip-promoting stresses were observed after a sudden increase in well rate in a Groningen-type gas reservoir.
- The described stress effect was observed to increase in magnitude for lower reservoir pressure, i.e. for reservoirs at a later stage of depletion.
- The effect is physical, but of a magnitude so small that unambiguous claims regarding earthquake triggering potential are difficult to make.
- The geometric irregularity of a fault with small displacement was found to cause concentrations of slip-promoting stress quickly exceeding those caused by the transient effects under primary investigation.

1 Introduction

We consider a subset of the broad category of earthquakes induced and/or triggered by anthropogenic injection or extraction of fluids in subsurface rock formations [*McGarr et al.*, 2002; *Shapiro*, 2015]. Industrial activities associated with this broad range of seismic events are the injection of waste water or CO_2 in deep aquifers [*Ellsworth*, 2013; *Shirzaei et al.*, 2016; *Zoback and Gorelick*, 2012], the production of oil or natural gas from subsurface reservoirs [*Segall*, 1989; *Van Wees et al.*, 2014; *Bourne et al.*, 2014], water injection in such reservoirs for improved oil recovery [*Raleigh et al.*, 1976], hydraulic stimulation ('fracking') of low-permeability reservoir rock for the production of shale gas [*Holland*, 2013; *Bao and Eaton*, 2016], and stimulation of natural fracture networks for geothermal energy production [*Baisch et al.*, 2006; *Deichmann and Giardini*, 2009].

In this broad category of fluid injection- or extraction-related seismic events, various mechanisms are at play. A first distinction concerns the source of energy released by the fault movement. This may be elastic rock deformation originating from plate tectonics ('triggered' earthquakes); or production-induced compaction or injection-induced expansion of reservoir rock ('induced' earthquakes). A second distinction concerns the location of the seismic event in relation to the reservoir into which or from which fluids are injected or extracted. Fault movement may be triggered in the reservoir itself, or in the overlying or underlying impermeable cap or base rock. A third distinction concerns the pathway for the propagation of pore pressure from the injection or production well to the fault. This may be a (predominantly) natural fracture network, as is the case for geothermal heat production from hot fractured rock, or a fracture network generated by hydraulically stimulating or 'fracking' relatively impermeable rock as applied in shale gas production. Alternatively, the pathway for pore pressure propagation may be (predominantly) the reservoir matrix, i.e. the permeable rock itself. This is often the case for oil or natural gas production from permeable clastic or non-fractured carbonate reservoirs, as well as for the injection of water or CO_2 in aquifers of a similar geological nature.

We restrict our analysis to the subset of induced earthquakes that originate from the reservoir itself, with a main pathway for pore pressure propagation formed by permeable rock with little to no fractures such that the flow is governed by Darcy's law. In particular, we consider earthquakes related to natural gas production that have been observed in the large Groningen gas field in The Netherlands [*Van Wees et al.*, 2014; *Bourne et al.*, 2014]. The field has estimated recoverable reserves of 2.8×10^{12} Sm^3, of which 2.0×10^{12} Sm^3 have been produced to date through a total of 258 wells distributed over 22 clusters. At the start of production reservoir pressure was 35 MPa, which has dropped to a current average pressure of around 7.5 MPa, although a differential pressure of approximately 3 MPa exists between the north and south of the field (approximately 45 km apart) because of a spatially phased development. Seismic activity with magnitudes above 1.5 M_L was not observed until the early 1990s, but over the past decade a steep increase in the number of events has occurred, with a maximum observed event of 3.6 M_L in 2012.

It is now generally accepted that most of the energy in the seismic events in the Groningen field results from compaction of the sandstone reservoir rock, although the release of additional seismic energy from naturally stressed faults deep below the reservoir has not been excluded. The most likely hypothesis is that compaction at both sides of a fault with a significant throw is the main reason for the build-up of strain energy that may be released when the shear stress in the fault reaches a critical limit caused by continuing compaction [*Mulders*, 2003]. Although the original reasoning was that the depletion of the field would lead to an increased magnitude of the compressive normal stresses over the faults and thus, according to the Coulomb failure criterion, to a decreased probability of seismic events, there is now sufficient evidence that the compaction-driven seismicity across faults as described above is indeed the main reason for the earthquakes observed in the field [*Zbinden et al.*, 2017].

The current seismic hazard model as applied by the operator is based on a statistical relationship between the cumulative compaction and the event rate [*Bourne et al.*, 2014]. Control measures, imposed at national government level and based on advice of the national regulatory authority (the State Supervision of the Mines) primarily involve reducing production rates field wide, and in particular at clusters where high event rates have been observed. Statistical analysis indicates that these production rate restrictions indeed show a correlation to a reduced event rate, although convincing evidence specifically indicating a direct causal relationship has yet to be put forward [*Van Thienen-Visser and Breunese*, 2015]. Furthermore, it has been hypothesized that another control measure could be the avoidance of fluctuations in well production rates, both in the form of sudden changes (production start-ups or close-ins) and in the form of seasonal fluctuations. In fact, the current government-imposed production controls are already based on this hypothesis: they limit the fluctuation of production rates to a minimum, but such that seasonal variations in domestic natural gas demand (notably increased production in cold winters) can be accommodated. This implies a flat production rate in combination with storage of excess gas in summer in a nearby depleted gas field which is now used as an underground gas storage facility.

In this study, we do not address the compaction mechanism leading to induced seismicity in the Groningen field, but instead consider the situation of a fault that is already critically, or almost critically, stressed such that a small perturbation of the local stress state may lead to triggering of an earthquake. In particular, we are interested in perturbations resulting from a sudden increase in production rate in a nearby well. This flow rate change will alter the pressure field in the reservoir causing various spatial and temporal pressure gradients in the reservoir which, in turn, result in changes in the state of effective stress.

Among others, *Wang* [2000]; *Shapiro* [2015] and *Cheng* [2016] present analytical 3D solutions of the propagation of pore pressures and stresses resulting from sudden rate changes in a point source for a poroelastic full-space, following the work of *Rudnicki* [1986] who, in turn, builds on results of *Cleary* [1977]. For a permeable reservoir of large spatial extent sandwiched between impermeable cap rock and base rock layers, an axially symmetric schematization appears more appropriate. Such (semi-)analytical solutions in cylindrical coordinates for the propagation of pore pressures around a line source or sink have been derived in various domains such as hydrology [*Theis*, 1935; *Jacob*, 1940; *Sternberg*, 1969; *Bear and Corapcioglu*, 1981; *Helm*, 1994; *Verruijt*, 2016], petroleum engineering [*Van Everdingen and Hurst*, 1949; *Clegg*, 1967; *Monfared and Rothenburg*, 2015a], geotechnical engineering [*Carter and Booker*, 1982], geomaterials [*Rudnicki*, 1986], and geophysics [*Segall*, 1989; *Segall and Fitzgerald*, 1998]. Several of these publications also consider the resulting stresses and/or strains in axial and/or radial directions using different solution methods (both direct and Laplace-transformed, the latter with either fully analytical or numerical inverse transforms). Importantly, they use a variety of assumptions regarding the domain extent (bounded vs. infinite), boundary conditions (constant rate vs. constant pressure) and deformation state (1D with axial or radial deformations only vs. 2D under plane stress or plane strain conditions). There are some publications in which it is attempted to justify the various assumptions with the aid of numerical simulations, i.a. [*Hsieh and Cooley*, 1995; *Monfared and Rothenburg*, 2015b].

For this study, the poroelastic response to a transient flow regime was modeled numerically using an efficient sequential FVM-FEM simulation strategy. We investigate an idealized Groningen-like geometry, solving for short time scales to capture the developing pressure field of a single producer and the stress changes it induces. The aim is to discover whether the hypothesised added risk of triggering induced seismicity exists, explore how some controllable and uncontrollable variables influence its severity, and possibly provide clues on how production strategy might be able to minimize risks in the future.

2 Poroelastic modeling

We consider an axially symmetric, laterally extensive, horizontally layered geometry modelled on the local geology of the Groningen gas field. Due to the compressibility contrast between pore fluid and reservoir rock, coupling of the flow problem to the geomechanical problem can be neglected. This enables the use of an efficient sequential FVM-FEM solution strategy in our dynamic reservoir simulator, in which the cell-centered pressure field acts as a known body force when solving for the vertex-centered solid displacements. These displacements can subsequently be used to determine the complete state of stress as a function of time and spatial coordinates.

2.1 Governing equations

2.1.1 Fluid flow

The basic governing equation of poroelasticity is the storage equation (1). It signifies mass conservation of both pore fluid and the solid matrix, and is obtained by adding both mass balance equations after normalizing them by the density of the conserved quantity they represent. Second order terms are dropped, assuming that the product of velocity and density gradient of each conserved quantity is negligibly small. It has a form resembling a classical diffusion equation in terms of pressure p, augmented with terms that account for the effect that deformation of the porous medium has on the flow problem.

$$\alpha \frac{\partial \varepsilon}{\partial t} + S \frac{\partial p}{\partial t} - \nabla \left(\frac{k}{\mu} \nabla p \right) = 0, \tag{1}$$

where ε is the volume strain, α is the Biot coefficient, S is the storativity and where the third term represents the total fluid flux with respect to the porous medium via Darcy's law. For a full derivation starting from conservation laws, refer to Appendix A.1.

If a large contrast exists between the fluid compressibility C_f and the compressibility of the (drained) porous medium C_m such that $C_\mathrm{m} = \frac{1}{K} \ll \phi C_\mathrm{f}$, the influence of solid deformation on the pressure solution can be safely neglected [*Cheng*, 2016; *Verruijt*, 2016]. The reverse does not hold, i.e. pore pressure changes must be taken into account when solving for solid displacements. This unilateral decoupling of flow from mechanics allows for the flow problem to be solved separately, after which the obtained pressure field enters the deformation problem as a known body force.

However, the assumption that second order terms can be neglected — although valid for slightly compressible fluids and low flow velocities — is generally untenable when describing the radial flow of gas, especially for the high flow rates that occur around a producing gas well. Fortunately, the decoupling allows us to rewrite the pore fluid mass balance as a diffusion equation without dropping these terms, by introducing a real gas pseudopressure as proposed by *Al-Hussainy et al.* [1966]:

$$m(p) = 2 \int_{p_\mathrm{ref}}^{p} \frac{k}{\mu_\mathrm{g}(p)} \frac{p}{Z(p)} \, \mathrm{d}p, \tag{2}$$

where Z is the real gas deviation factor and p_ref is a sufficiently low reference pressure, chosen such that it is always beneath the lowest pressure in the system. Using the real gas equation of state, the fluid mass balance equation can be rewritten in terms of p and Z. Assuming Darcy flow, constant porosity and isothermal conditions, a change of variables to $m(p)$ gives the following (nonlinear) diffusion equation:

$$\frac{\phi \mu_{\mathrm{g}}(p) C_{\mathrm{g}}(p)}{k} \frac{\partial m}{\partial t} - \nabla^2 m = 0\,, \tag{3}$$

which describes the flow of gas without assuming small density gradients and low flow rates, whilst fully incorporating the pressure-dependent fluid properties. The pseudopressure $m(p)$ is precomputed to a desired degree of accuracy using numerical integration, so that upon obtaining a solution for m, the real pressure solution p can be obtained by linear interpolation without introducing significant extra errors. For a detailed derivation of (3), refer to Appendix A.2.

2.1.2 Solid mechanics

The displacement problem must satisfy the equations of mechanical equilibrium, which follow from Newton's laws of motion when the second derivative of the displacement vector $\mathbf{u}$ with respect to time (i.e. the change in momentum) is assumed to be negligible:

$$\boldsymbol{\nabla} \cdot \boldsymbol{\sigma} - \mathbf{f} = \mathbf{0}, \tag{4}$$

where $\boldsymbol{\sigma}$ is the second order Cauchy stress tensor and $\mathbf{f}$ represents the body forces in all coordinate directions, if present. Following the convention used in soil mechanics, normal stresses are positive for compression, and a shear stress σ_{ij} is positive when it applies force in a direction along j of opposite sign compared to the component n_i of the unit vector normal to the surface on which it acts. Besides the equations of equilibrium, the problem must satisfy the strain-displacement relations (or compatibility equations):

$$\boldsymbol{\varepsilon} = \frac{1}{2} \left[\boldsymbol{\nabla} \mathbf{u} + (\boldsymbol{\nabla} \mathbf{u})^T \right], \tag{5}$$

where $\boldsymbol{\varepsilon}$ is the infinitesimal strain tensor. Lastly, stress and strain are linearly related via Hooke's law in the constitutive relations:

$$\boldsymbol{\sigma} = \mathbf{C} : \boldsymbol{\varepsilon}\,, \tag{6}$$

where $\mathbf{C}$ is a rank four stiffness tensor. For a three-dimensional isotropic material, this amounts to 21 equations in total (6 equilibrium equations, 9 strain-displacement relations and 6 independent constitutive equations), one for each of the unknowns (3 displacements, 9 stresses and 9 strains). For the full set of elastic equations expanded in an axially symmetric cylindrical coordinate system adapted from *Verruijt* [2016], refer to Appendix A.3.

2.2 Numerical solution

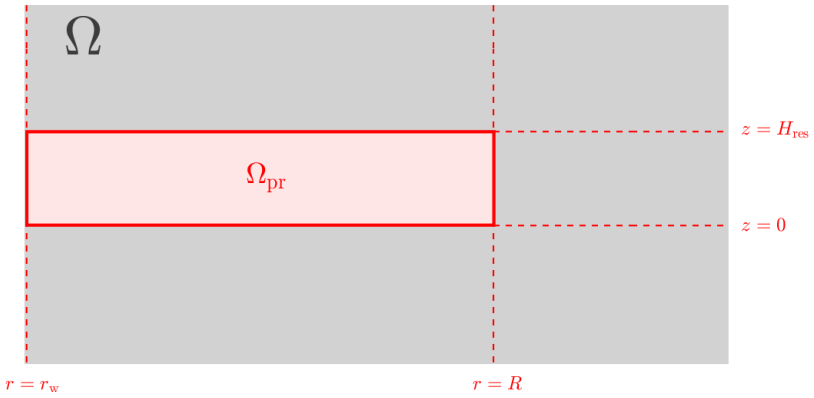

Figure 1: *Subdomain Ω_{pr} embedded within the complete system Ω, which extends further in the positive radial and both vertical directions.*

Simulations were conducted in Matlab using an algorithm adapted from *Chessa* [2002] for an unstructured triangular grid, which is initialized using Matlab's built-in Delauney-type meshing algorithm and finished by alternating steps of refinement and node coordinate adjustment to improve triangle shape. The pseudopressure problem is solved on only part of the domain, chosen as a section of the reservoir interval of an extent such that flow remains infinite-acting during simulation. An especially high grid cell resolution is chosen in this region to fully capture the developing pressure field. To our knowledge, this sequential strategy using real gas pseudopressure has not been described in literature. Derivations and algorithms can be found in the appendix, which details the discretisation of both the flow problem (Appendix B.1) as well as the displacement problem (Appendix B.2). Furthermore, it contains a validation study of the obtained pressure solution (Appendix C), and a pseudocode description of simulator algorithms (Appendix E).

2.2.1 Pressure field

Given that the reservoir is in a transient flow regime, at each time t after the start of production there exists a radius r beyond which the disturbance has not yet had time to travel, i.e. pressure is still constant at $p = p_{\mathrm{res},0}$. For sake of computational efficiency, we choose a radius $r = R$ bounding the subdomain Ω_{pr} outside of which the diffusivity equation (3) need not be solved. Within Ω_{pr}, a high grid cell resolution enables us to capture the steep gradients of the developing pressure field. The problem is discretised in time using backward differences to ensure numerical stability. Discretisation in space is achieved with the finite volume method, Ω_{pr} being divided into $n_{\mathrm{e,pr}}$ grid cells each containing a discrete pseudopressure unknown m_k. Pseudoflow across cell faces is described using a two-point flux approximation as decribed by *Karimi-Fard et al.* [2003]. Grouping of terms results in a nonlinear system of $n_{\mathrm{e,pr}}$ equations for which Picard iteration was found to be of sufficient computational efficiency.

2.2.2 Solid displacements & state of stress

The mechanical problem is then solved across the entire domain Ω using the Galerkin method of weighted residuals, with discrete unknowns $u_{r,i}$ and $u_{z,i}$ at each of the n_{n} nodes, located at triangle vertices. Making use of the linearity of the problem, the effect of pres-

sure changes in the reservoir is incorporated by assigning every element l a pressure drop Δp_l, with $\Delta p_l = p_{k_l} - p_{\text{res},0}$ for each element on Ω_{pr} and zero otherwise.

Upon solving for the displacement field, the state of stress can be computed using the compatibility equations (5) and Hooke's law (6). As the displacement gradients (and consequently the stress components) are generally not continuous across cell boundaries, the average state of stress in an element is chosen as a representative value. Using direction cosines, the reference frame can be rotated to find the stress components acting on a hypothetical plane at a given angle. A derivation of the transformation matrices can be obtained from Appendix A.4.

To assess the potential for triggering of production-induced seismicity, we use the Coulomb stress $\tau_c = \tau_s - \mu_f \cdot \sigma'_n$, with μ_f the coefficient of friction, σ'_n the effective normal stress acting on the fault and τ_c the magnitude of the shear stress promoting fault slip. Given the employed sign convention and the fact that Groningen is in a normal faulting regime, this implies a sign change when assessing faults dipping towards the producer.

2.3 Reservoir model

2.3.1 Geometry & rock properties

Numerical experiments were performed for an axially symmetric, horizontally layered geometry, with the producing interval sandwiched between impermeable overburden and basement. Stratigraphy was based on the geology of the gas-producing regions of the northern Netherlands.

Elastic and hydromechanical properties were obtained from the technical addendum to the field development plan published by the operator responsible for extraction of oil and gas in the Netherlands [*NAM*, 2016]. Elastic properties are constant within stratigraphic intervals, and the producing interval was modeled with a homogeneous permeability ($k = 5 \cdot 10^{-14}$) and porosity ($\phi = 0.15$).

Zero-displacement boundary conditions were applied at the proximal and bottom domain boundaries in radial and vertical directions, respectively. All other boundary conditions were left stress-free. Lateral extent of the whole geometry and vertical extent of the modeled underburden were chosen such that a further increase in size no longer influenced the outcome of numerical experiments.

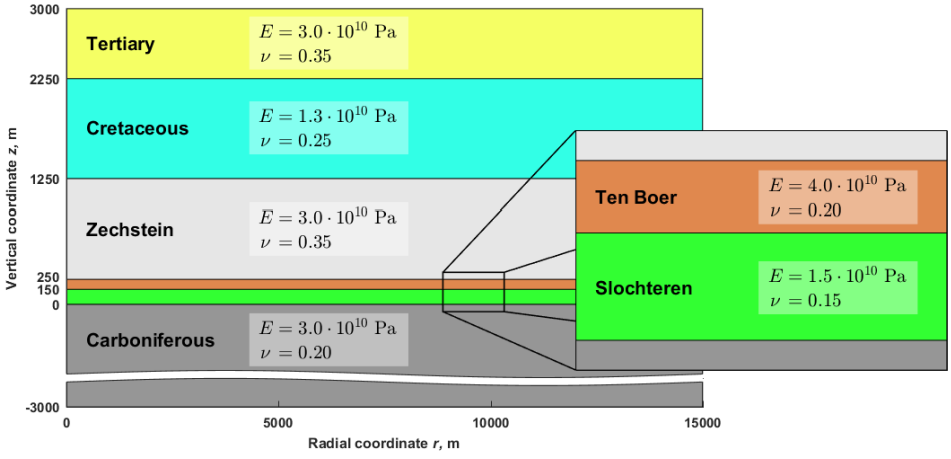

Figure 2: *Horizontally layered stratigraphic model with corresponding elastic parameters.*

2.3.2 Fluid properties

The pore fluid was modeled as a gas mixture typical for the Groningen field, with specific gravity $\gamma_g = 0.65$ and a methane content of around 80%. Pressure-dependent properties of reservoir fluids are usually best described by empirical correlations relating them to pseudo-reduced temperature T_{pr} and pseudo-reduced pressure p_{pr}, computed by normalizing pressure and temperature with their respective critical values T_{pc} and p_{pc}. Pressure-dependent gas viscosity μ_g was modeled using Lucas' approximation [*Lucas*, 1981] to the correlation charts put forwards by *Carr et al.* [1954], valid for $1 < T_{pr} < 40$ and $0 < p_{pr} < 100$. The explicit correlation proposed by *Azizi et al.* [2010] (valid for $1.1 < T_{pr} < 2$ and $0.2 < p_{pr} < 11$) was used to compute the real gas deviation factor Z as a function of pressure. Besides its accuracy, its explicit nature allows it to be differentiated to derive an analytical expression for the pressure-dependent isothermal compressibility C_g.

3 Results

3.1 Induced stresses for semi-steady state production at long time scales

Theoretically, the decrease in pore pressure caused by extensive field-wide depletion of a gas reservoir causes effective normal stresses to grow in magnitude, thereby inhibiting slip on existing fault planes. However, geometric irregularities, even relatively small ones such as a fault with a throw of only a few percent of total reservoir height, can cause local concentrations of slip-promoting stresses that grow in magnitude as depletion progresses. These induced stresses may cause existing faults to reach critical stress levels even in a geologically inactive region such as Groningen, with the potential to release the built up strain energy in the form of an earthquake when triggered either by continued depletion or some perturbation of the stress field, small or large.

To investigate the elastic response of field-wide production at long time scales, a laterally extensive reservoir ($r_e = 1.5 \cdot 10^4$ m) was subjected to a uniform pressure drop of 10.0 MP, as if depleting at a semi-steady state. The reservoir contained a fault dipping towards the producer at $\theta = 85°$ with a throw of 5% of total reservoir height. It should be noted that due to the radially symmetric description of the problem, this constitutes a fault that forms part of a conical surface wrapped around the producer. Although unphysical geometrically, the behaviour of such a system can still provide trends which may apply qualitatively to scenarios of stress concentrations near planar faults as well.

Sharp re-entrant corners are known to cause singularities in the solution of elliptic PDE's [*Williams*, 1952], leading to unbounded stresses which, in real life, would plastically deform the material. To prevent this effect from dominating the results, re-entrant corners were rounded off. Slip-promoting shear stresses were observed to concentrate around the geometric irregularities, confirming the observations of *Mulders* [2003].

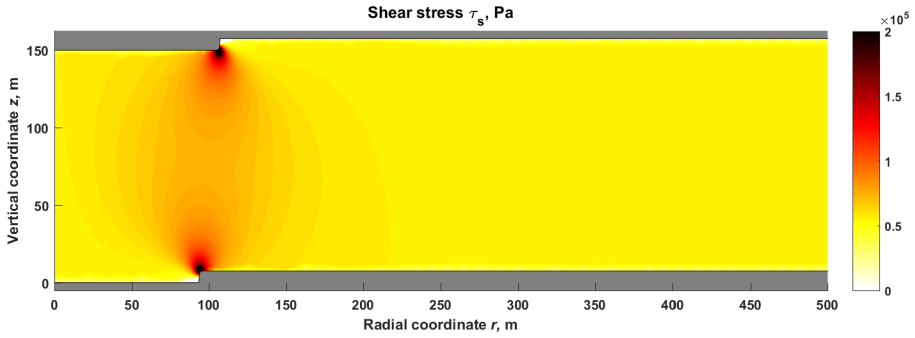

Figure 3: *Shear component of Coulomb stress under uniform depletion of* 10.0 *MPa.*

Plotting the Coulomb stress and its components in the area worst affected as a function of the pressure drop $-(\Delta p)$, we observe that stress components increase in magnitude in a ratio $(\mu_f \cdot \sigma'_n)/\tau_s < 1$, causing Coulomb stress to increase as well (figure 4)

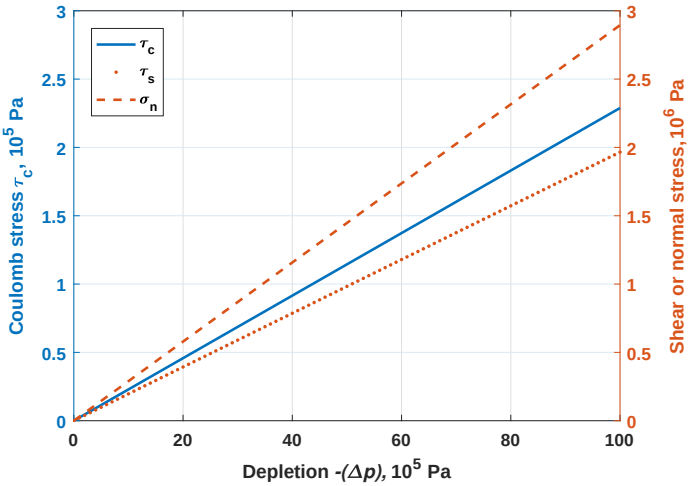

Figure 4: Coulomb stress and its components in the location where the former is highest, plotted versus pressure drop.

3.2 Transient baseline scenario

As a base case, we consider the scenario of a disk-shaped gas reservoir at a constant initial pressure $p_{res,0} = 7.5$ MPa, comparable to current pressures found in Groningen. At the start of production, a rate constraint of $q_{sc} = -3.0 \cdot 10^6$ m^3/day is applied instantaneously to the proximal boundary of the producing interval. Using a timestep Δt of 15 minutes, simulations model the first 5 days of production.

3.2.1 *Pressure field*

Figure 5 visualizes the development of the pressure field during the first 5 days of production, showing that flow is still infinite-acting. The subdomain Ω_{pr} is modeled with a radius R = 2500 m, in which this transient regime can be modeled for up to 20 days.

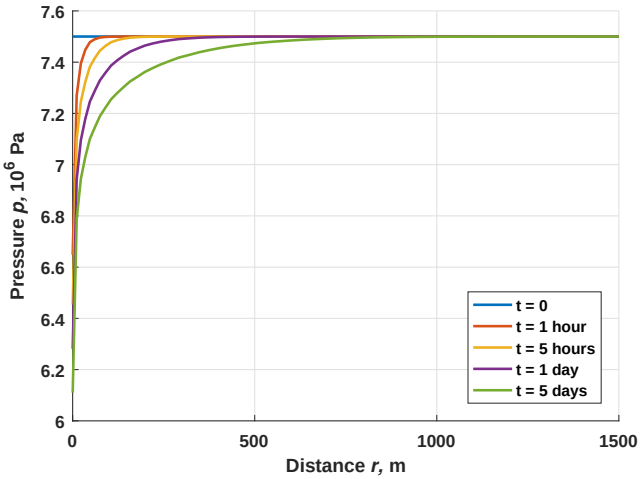

Figure 5: Developing pressure field during the first 5 days of production.

3.2.2 *Displacements*

As pore pressure in de reservoir diminishes, effective stresses change and the reservoir deforms. For larger time scales with field-wide pressure drops, displacement in the negative z-direction tends to dominate: the overburden can subside as one unit with minimal strain while the basement has no free surface enabling this behaviour. At short times however, we can still observe that positive vertical displacement at the bottom of the reservoir is of the same order of magnitude (figure 6). The reason for this is that, as the pressure disturbance has only travelled a small distance into the reservoir, the arching effect works to prevent vertical displacement [*Mulders*, 2003].

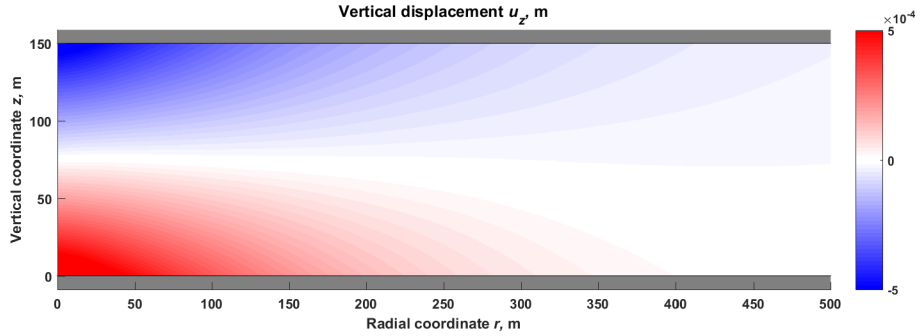

Figure 6: *Vertical displacement field after 1 day of production.*

Unlike the vertical displacement, the radial displacement is not monotonous along the radial axis for an infinite-acting flow regime: a state of relative compression is found near the wellbore, changing to relative extension with increasing radial coordinate (figure 7).

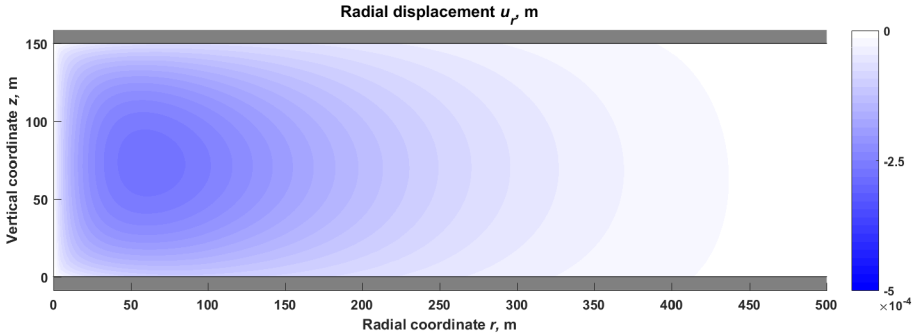

Figure 7: *Radial displacement field after 1 day of production.*

3.2.3 Stress field

Plotting the Coulomb stress on a fault dipping towards the producer at $\theta = 85°$ as a function of both spatial coordinates, Coulomb stress is found to concentrate at the top of the reservoir (figure 8). Conversely, Coulomb stresses on faults dipping away from the producer show elevated levels local to the bottom of the reservoir. This is due to the different sign of shear stress on both vertical boundaries, as well as to an asymmetry in the relative magnitude of shear and normal stresses caused by rotating the reference frame. Due to the nature of the trigonometric functions required for the transformation, the assymetry decreases for decreasing dip angles, vanishing for $\theta = 60°$ after which further decrease of θ causes the same asymmetry to develop on the other side.

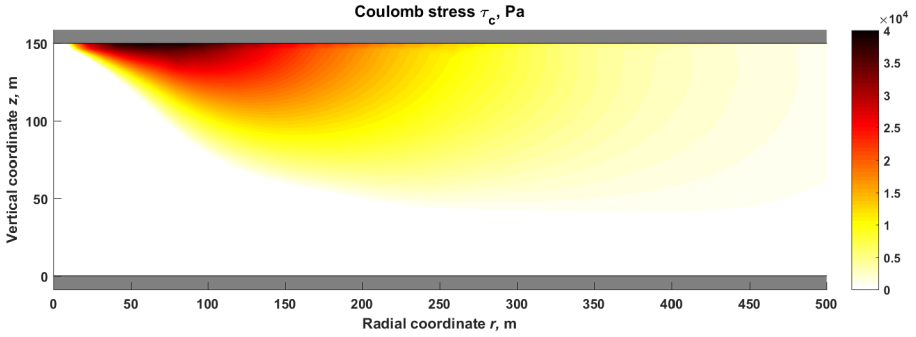

Figure 8: *Coulomb stress for slip along a fault plane dipping towards the producer at $\theta = 85°$ at an arbitrary location, $t = 1$ day.*

Knowing that the state of stress is most conducive to fault slip at either the top or bottom of the reservoir interval, the Coulomb stress can be visualized as function of time and radial coordinate by only looking at the high-risk zone (figures 9 & 10). After ap-

proximately a day of production, the Coulomb stress exhibits a local maximum around $r = 100$ m. This location then remains the spatial maximum as production continues and the pressure field stabilizes.

To facilitate comparison of Coulomb stress responses when changing the value of a certain parameter, a two-dimensional dataset was created by plotting τ_c only for that radial coordinate r where the maximum occurs. Figure 11 shows the result for the stress field described above, as well as the components of normal and shear stress from which it is derived. It becomes clear that the (sudden) increase in Coulomb stress arises because, although the shear contribution immediately grows in magnitude, the initial change in effective normal stress (due to elastic coupling) is one of relative tension. Starting from the moment at which the pressure disturbance arrives, the drop in pore pressure makes a compressive contribution to effective normal stress σ_n. Eventually, compressive stresses come to dominate the tensile stress transferred via the rock matrix, stabilizing the Coulomb stress (figure 12).

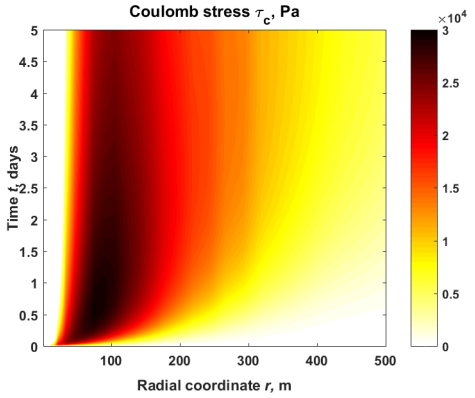

Figure 9: Coulomb stress versus time t and radial coordinate r at the top of the reservoir, for a plane dipping towards the producer at $\theta = 85°$, first five days.

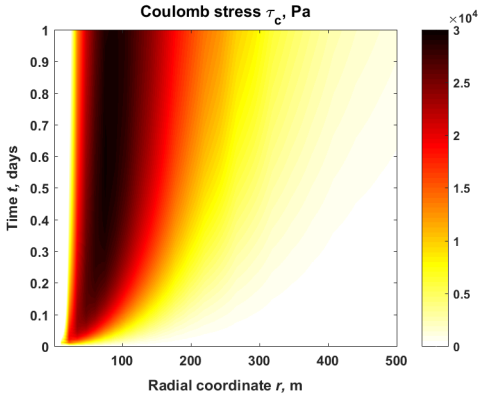

Figure 10: Coulomb stress versus time t and radial coordinate r at the top of the reservoir, for a plane dipping towards the producer at $\theta = 85°$, first day.

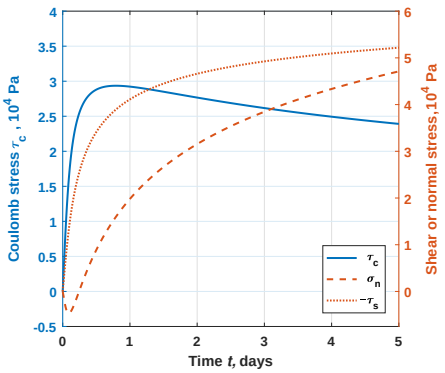

Figure 11: Coulomb stress and its components during the first five days of production, note the initially tensile σ_n.

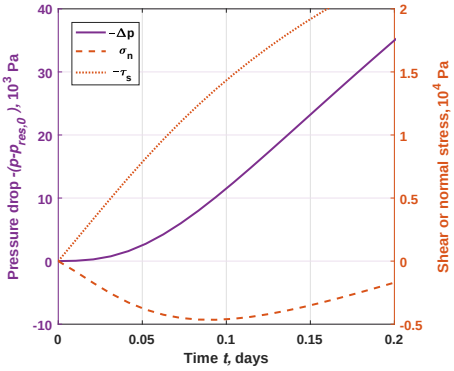

Figure 12: Stress components superimposed on pressure drop during the first 0.2 days of production.

3.2.4 Dependence of Coulomb stress on fault orientation

To explore the influence of fault orientation on both the magnitude and prominence of the local maximum in Coulomb stress, simulations were conducted for various dip angles and directions, again assuming normal faulting. Faults in the Groningen field are often especially steep, with dip angles generally around 80° and seldomly below 70° [*NAM*, 2016]. Figure 13 shows the variation of Coulomb stress response, which exhibits an upward trend in both magnitude and prominence of the local stress maximum for increasing dip angles, as well as an increasing asymmetry between the different dip directions. As very large dip angles (i.e. near-vertical faults) are not uncommon and this orientation shows the strongest response, a fault dipping towards the producer at $\theta = 85°$ is selected as the subject of further numerical experiments.

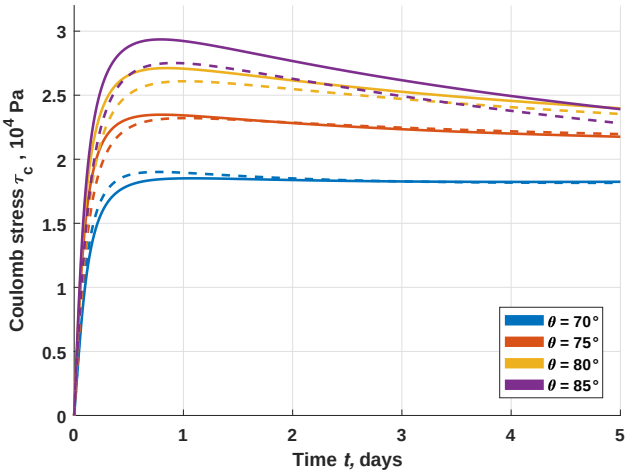

Figure 13: Coulomb stresses for various dip angles. Solid lines dip towards the producer, dashed lines dip away from the producer.

3.3 Production rate

Lowering production rates is often viewed as a seemingly obvious way of mitigating earthquake risk. Figure 14 shows the Coulomb stress response for different production rates, indeed showing greater stress levels for higher well rates. In fact, both peak stress and the stabilizing tails of the curve appear roughly proportional to the applied well rate. Separating the Coulomb stress into its normal and shear components, it becomes clear that the increased Coulomb stress can be ascribed mostly to a greater shear stressing rate caused by the steeper pressure gradients required to satisfy the production constraint. Although normal stress drops to a lower minimum for higher production rates, the timing of this minimum and the moment when the pore pressure drop succeeds in bringing back a state of relative compression remains the same.

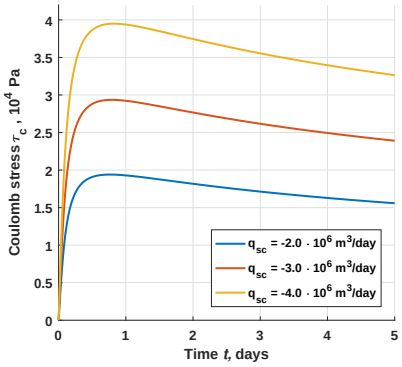

Figure 14: Coulomb stress for an increasing magnitude of the well rate.

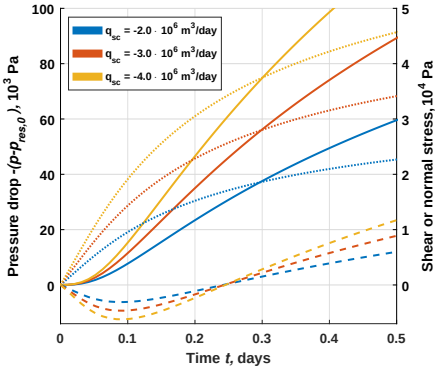

Figure 15: Shear component (dotted) and normal component (dashed) superimposed on pressure drop for the first 0.5 days of production.

3.4 Production ramping

An instantaneous switch in well rate to operating levels is hypothesized to increase the risk of triggering earthquakes compared to a more gradual approach, i.e. either moving to operating rates in two or more discrete steps or in a continuous rate-buildup, both of which can be applied in a shorter or longer time window. Both parameters were varied separately to study their effect on stress levels, choosing the moment at which production commences such that the total amount of gas produced is equal when the ramping phase is complete. In both cases, the stress levels appeared to remain below or equal to the stresses found for an instantaneous switch to operating rate, the curves meeting up as their respective pressure fields begin to align. For the case of a varying number of pressure increments within the same time window (figure 16), the maximum Coulomb stress was observed to be slightly lowered as the number of increments increases. However, this change seems to be governed only by the amount of extra time taken to reach the operating rate. Indeed, increasing the time Δt between the onset of production and the moment that operating rates are reached, moves the maximum Coulomb stress along the descending curve, with a time offset that seems proportional to Δt.

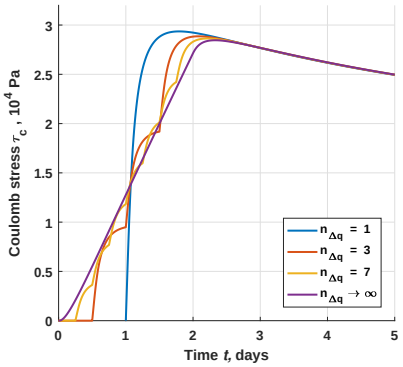

Figure 16: Coulomb stress for an increasing number of well rate increments.

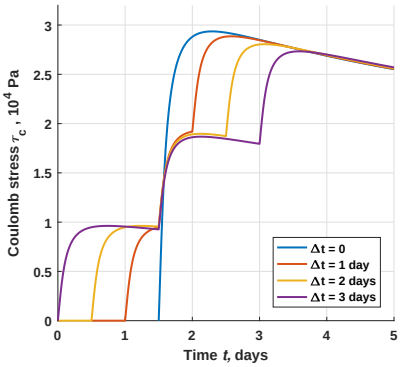

Figure 17: Coulomb stress for an increasing total ramping time.

3.5 Reservoir pressure

The frequency with which production-induced seismic events occur in the Groningen gas field has seen a very sharp increase over the past decades; a trend that might be explainable in part by ever-increasing levels of compaction and the corresponding straining of faults in the reservoir, as well as by various non-linear deformation effects not modelled in this study. In terms of the transient effect that is studied here, the variable of interest is the initial reservoir pressure $p_{\mathrm{res},0}$: not only does pressure have a large influence on the hydromechanical properties of the pore fluid, a lower reservoir pressure (i.e. a lower gas density) means that at in-situ conditions a larger volume of pore fluid needs to be displaced to achieve a certain production rate in terms of standard cubic meters. Numerical experiments were conducted producing at an equal rate q_{sc} for various reservoir pressures, and Coulomb stress levels were observed to increase dramatically (figure 18). Decomposition into shear and normal components (figure 19) reveals that this is caused largely by the increased time lag of the arriving pressure wave, in turn caused by the lower compressibility C_{f}. This causes the moment at which the minimum normal stress is reached to appear much later, during which time the shear component freely causes Coulomb stress to continue rising steeply.

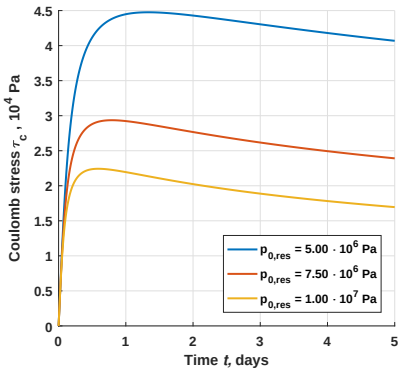

Figure 18: Coulomb stresses in reservoirs of different initial pore pressure.

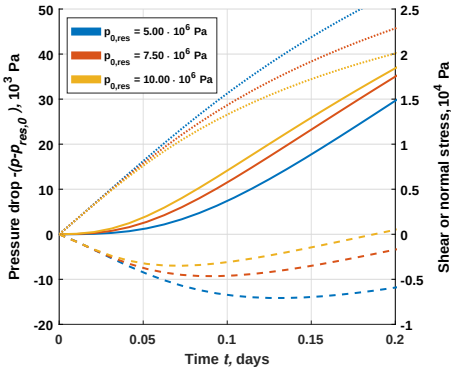

Figure 19: Shear component (dotted) and normal component (dashed) superimposed on pressure drop for the first 0.2 days of production.

3.6 Fault throw

To investigate the effect of a structural feature such as a fault with nonzero displacement, a fault dipping towards the producer at $\theta = 85°$ was positioned at $r = 100$ m, with a normal throw of 5% relative to the total height of the reservoir. A small throw is chosen so as not to alter the pressure field significantly through the reduction in radial flow area, as that would make comparison to other scenario more difficult. Moreover, the conical fault would exhibit exceedingly different pressure behaviour compared to a geologically realistic scenario.

After a day of production, it can already be observed that stress concentrations appear around the geometric irregularity (figure 20), with both a region of elevated and lowered Coulomb stress. Plotting the stress state at the radius of maximum Coulomb stress through time (figure 21), we find that for the displaced scenario, Coulomb stress at this point is monotonously increasing to levels above the local maximum found in the base case. Examining the shear and normal stresses separately (figure 22) reveals that both shear and normal stresses grow at a higher rate for the displaced fault, with the former evidently dominating. It is also observed that normal stresses become compressive faster in the displaced case, which is why the base case shows a higher Coulomb stress for the first 30 hours of production. Comparison of the local pressure drops for both scenarios shows a near perfect match. Numerical experiments for 20 days of production show a continuation of the trends observed after 5 days, with Coulomb stresses declining for the base case and slowly rising for the displaced fault. It should be noted that this increasing Coulomb stress is observed only locally, with surrounding regions behaving rather more like the base case.

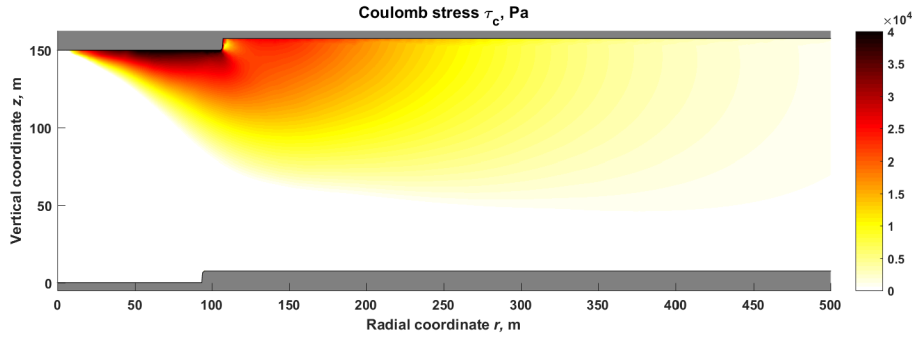

Figure 20: *Coulomb stress for a fault with a 5% throw relative to reservoir height, t = 1 day.*

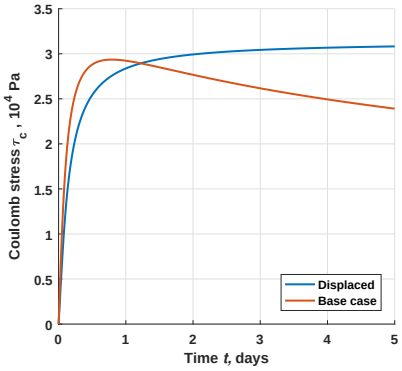

Figure 21: Coulomb stresses found for a fault with a 5% throw compared to the base scenario.

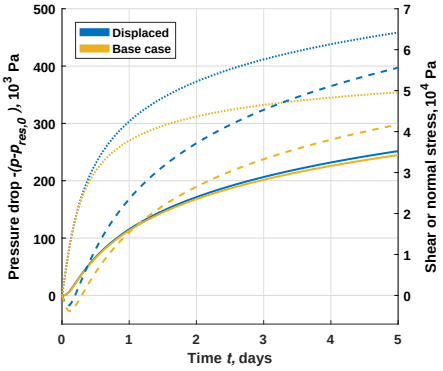

Figure 22: Shear component (dotted) and normal component (dashed) superimposed on pressure drop.

4 Discussion

The reservoir model used in this study is a simplified one, assuming linear elastic behaviour, homogeneity in rock properties and a single pore fluid phase. While complex real-world subsurface systems will produce at best quantitatively different outcomes, the idealized description used in this study provides insight into the mechanisms behind some of the obtained results.

4.1 Existence and mechanisms of transient stress effects

The phenomenon that a sudden change in well rate causes an extra stress effect that may trigger seismicity [*Segall and Lu*, 2015; *Shapiro et al.*, 2013] was indeed observed: Coulomb stresses showed a local maximum in both time and space. The existence and location of the spatial maximum can be explained in the vertical dimension by the importance of the sign of the shear component and the fact that shear stresses are greatest on the vertical limits of the reservoir. The reason for the maximum in the radial dimension is that the region of highest shear (i.e. close to the wellbore) is also the region of highest normal stress, with normal stresses rising to very high levels as r approaches r_w. This trade-off

means that for higher friction coefficients μ, the spatial maximum will likely move to a location more distal from the wellbore.

The explanation for the temporal maximum became evident when the shear and normal components of stress were observed separately, as elastic coupling of the rock matrix initially causes a state of relative tension to exist in the region where pore pressure has not yet dropped. This phenomenon can also explain why more steeply dipping faults show the strongest transient effect, both in terms of magnitude and prominence. The asymmetry with respect to dip direction is caused by the asymmetry of the state of shear stress σ_{rz}: the upper half of the reservoir exhibits greater stress magnitudes than the bottom due to the different elastic properties found in the under- and overburden. As dip angle increases, this asymmetry should become more evident in the Coulomb stress, as is indeed observed.

It should be noted that the effects described seem fundamental, and not an artefact of the idealized geometry or discretization of the problem. In terms of unincorporated physics, the simplified linear elastic description of the system is an approach widely used for time scales and deformations exceeding ours by several orders of magnitude. The assumption that $\frac{1}{K} \ll \phi C_\mathrm{f}$ was monitored and satisfied for all simulations. Taking all this into account, we have no reason to assume that the effects described will not also occur in a real reservoir setting. A sensitivity study, which separately altered the elastic moduli of the reservoir or the surrounding rock, showed that the effect of increased Coulomb stress increased for more elastic reservoir rock and more stiff surroundings (Appendix D).

Although the transient stress effects were indeed observed in our simulations, magnitudes of Coulomb stress, and also of its two components, were in the order of 10^4 Pa. This appears rather small – especially when compared to the ambient stress levels, which are three orders of magnitude higher. Even assuming faults are already critically stressed, these magnitudes beg the question whether they can be considered significant. As production time increases, the magnitude of the two components of Coulomb stress will continue increasing, possibly arriving at a point where even though Coulomb stress is lower than after the first day of producing, its two components reach magnitudes of significance.

Moreover, a geometric irregularity in the form of a fault with a relatively small displacement caused (Coulomb) stress concentrations of a magnitude that quickly exceeded the local maximum found for the disk-shaped geometry, still climbing monotonously after 20 days of production. It seems that these areas where stresses reliably build up in dangerous ratios are more likely candidates for triggering seismic activity. This is in addition to the fact that exactly in these regions stress build-up to critical magnitudes is believed to occur as a result of prolonged production.

4.2 Evaluation of observed stress magnitudes

Nucleation of an earthquake is a chance event, involving failure mechanisms that operate locally at very small length scales. Consequently, the question whether or not a given change in stress state in a certain location (small or large) will trigger seismicity is one that is difficult to answer, especially given the fact that the degree of uncertainty concerning the properties of a system can be enormous.

Dieterich [1994] proposes a seismic model that estimates the rate of earthquake nucleation based on a set of several state variables that each incorporate some physical aspect of earthquake formation. A key aspect of the model is that it relates seismicity to the rate at which Coulomb stress changes, not just on its magnitude. *Segall and Lu* [2015] put forward a way to simplify the model originally proposed by Dieterich, defining a rate of earthquake production R relative to a background rate (which may be very low in geologically inactive regions). This results in a single differential equation dependent on stressing rate, background stressing rate, ambient stress levels and a few physical parameters, pro-

viding a way to judge a stress path in terms of the potential for triggering seismicity. A derivation is not given in the original paper, but can be obtained from Appendix A.5.

As background stressing rates in Groningen are very low and ambient stress levels are in the order of 10^7 Pa, relative rates of earthquake production returned by the seismic model follow practically the same trends as those observed for Coulomb stress. As an example, figures 23 and 24 compare the relative rates R found for the base case and the scenario with decreased initial reservoir pressure $p_{\mathrm{res},0}$. The discrepancy between this result and the transient effect described by *Segall and Lu* [2015] is striking, but the characteristics of the two systems under investigation explain the difference. Chief among these is the fact that the other study dealt with injection of the more viscous water into a formation with permeability in the order of 10^{-16} m^2, requiring pressure differences in the order of 10^7 Pa, much greater than the ones observed for our gas reservoir.

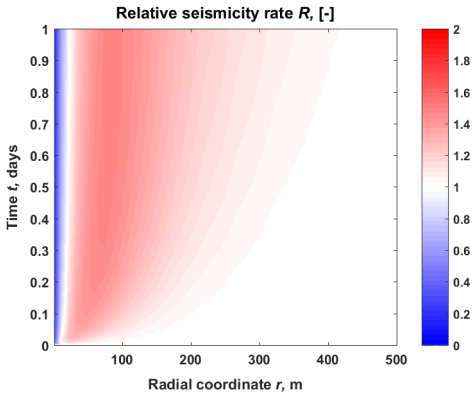

Figure 23: Seismicity rates obtained for the base case.

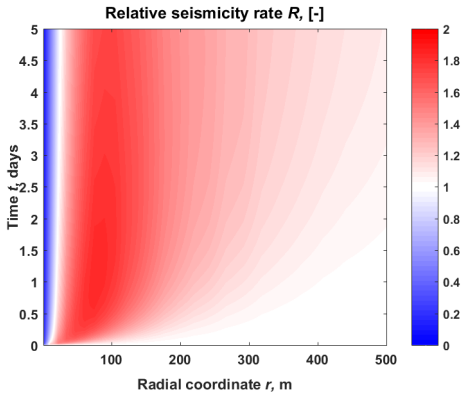

Figure 24: Seismicity rates obtained for $p_{\mathrm{res},0} = 5.0 \cdot 10^6$ Pa.

5 Conclusions

- A hypothesized transient maximum in slip-promoting stresses following a sudden increase in production rate is observed in our simulations.
- The underlying cause is the time required for the pressure disturbance to reach a certain radius, during which the comparatively instantaneous elastic coupling through the rock matrix induces a state of relative radial tension and growing shear stress. As pore fluid pressure drops, effective normal stresses become compressive and subsequently grow to first stabilize and then lower the Coulomb stress.
- The effect is strengthened with increasing dip angle, increasing well rate and decreasing reservoir pressure.
- A gradual or stepwise build-up to the operating rate was observed to lower the maximum Coulomb stress, with a larger time window being of much greater value than an increased number of rate increments.
- Although showing the described behaviour, both Coulomb stress and its components appear small to the point of insignificance, with ambient stresses exceeding them by three orders of magnitude.
- A seismic model based on rate-and-state friction predicted a very weak increase in seismic activity, such that unambiguous claims on the potential for triggering an earthquake are difficult to make.
- A small geometric irregularity in the form of a fault with a 5% throw relative to reservoir height caused (Coulomb) stress concentrations to quickly and monotonously build up to levels far exceeding the observed maximum in the disk-shaped reservoir, making those regions more likely candidates for triggering slip on an existing fault.

A: Derivations

A.1 Storage equation for slightly compressible fluids

The storage equation for slightly compressible fluids (in which the coupling of flow and mechanics is significant) is derived by adding the fluid and solid mass balances in a control volume, after which the principle of effective stress is used to group the terms expressed in derivatives of pressure and volumetric strain. Both fluid and solid are assumed linearly compressible. Furthermore, it is assumed that porosity is constant and the product of density gradient and velocity is negligibly small. Derivation is a more detailed version of the one presented by *Verruijt* [2016].

A.1.1 Fluid mass balance

The basic conservation equation is a generalised fluid mass balance in a porous medium with zero source:

$$\frac{\partial\left(\phi\rho_{\mathrm{f}}\right)}{\partial t}+\nabla\left(\rho_{\mathrm{f}}\phi\mathbf{v}_{\mathrm{f}}\right)=0\,. \tag{A.1}$$

Rewriting the time derivative in terms of pressure, one obtains

$$\frac{\partial\left(\phi\rho_{\mathrm{f}}\right)}{\partial t}=\phi\frac{\partial\rho_{\mathrm{f}}}{\partial p}\frac{\partial p}{\partial t}=\phi\rho_{\mathrm{f}}\,C_{\mathrm{g}}\,\frac{\partial p}{\partial t}\,, \tag{A.2}$$

and application of the chain rule to expand the second term gives

$$\nabla\left(\rho_{\mathrm{f}}\phi\mathbf{v}_{\mathrm{f}}\right)=\rho_{\mathrm{f}}\nabla\left(\phi\mathbf{v}_{\mathrm{f}}\right)+\underbrace{\phi\mathbf{v}_{\mathrm{f}}\nabla\rho_{\mathrm{f}}}_{\text{negligible}}\,. \tag{A.3}$$

These expressions are substituted in (A.1) and divided by the fluid density ρ_{f} to find:

$$\phi C_{\mathrm{g}}\frac{\partial p}{\partial t}+\nabla\left(\phi\mathbf{v}_{\mathrm{f}}\right)+\underbrace{\frac{\phi\mathbf{v}_{\mathrm{f}}}{\rho_{\mathrm{f}}}\nabla\rho_{\mathrm{f}}}_{\text{negligible}}=0\,. \tag{A.4}$$

A.1.2 Solid mass balance

Again, one starts from a generalised mass balance of a porous medium with zero source:

$$\frac{\partial}{\partial t}\Big[(1-\phi)\rho_{\mathrm{s}}\Big]+\nabla\Big[(1-\phi)\rho_{\mathrm{s}}\mathbf{v}_{\mathrm{s}}\Big]=0\,. \tag{A.5}$$

Using the fact that matrix density is a function of pressure and isotropic total stress, we find

$$\frac{\partial\rho_{\mathrm{s}}}{\partial t}=\frac{\rho_{\mathrm{s}}C_{\mathrm{s}}}{1-\phi}\left(\frac{\partial\sigma}{\partial t}-\phi\frac{\partial p}{\partial t}\right)\,, \tag{A.6}$$

in addition to which the second term in (A.5) is expanded using the chain rule:

$$\nabla\left[(1-\phi)\rho_s \mathbf{v}_s\right] = \rho_s \nabla\left[(1-\phi)\mathbf{v}_s\right] + \underbrace{(1-\phi)\mathbf{v}_s \nabla\rho_s}_{\text{negligible}}. \tag{A.7}$$

Lastly, the former two expressions are substituted in (A.5) and divided by ρ_s to give

$$C_s\left(\frac{\partial\sigma}{\partial t} - \phi\frac{\partial p}{\partial t}\right) + \nabla\mathbf{v}_s - \nabla\phi\mathbf{v}_s + \underbrace{\frac{(1-\phi)\mathbf{v}_s}{\rho_s}\nabla\rho_s}_{\text{negligible}} = 0\,. \tag{A.8}$$

A.1.3 Storage equation

Adding the fluid and solid mass balances while dropping the negligible terms leaves

$$\nabla\mathbf{v}_s + \nabla\left[\phi(\mathbf{v}_f - \mathbf{v}_s)\right] + \phi\left(C_g - C_s\right)\frac{\partial p}{\partial t} + C_s\frac{\partial\sigma}{\partial t} = 0, \tag{A.9}$$

upon which substitution from the definitions

$$\varepsilon = \nabla\mathbf{u}, \tag{A.10}$$

$$\frac{\partial\varepsilon}{\partial t} = \nabla\mathbf{v}_s, \tag{A.11}$$

$$\mathbf{q} = \phi\left(\mathbf{v}_f - \mathbf{v}_s\right), \tag{A.12}$$

gives:

$$\frac{\partial\varepsilon}{\partial t} + \phi\left(C_g - C_s\right)\frac{\partial p}{\partial t} + C_s\frac{\partial\sigma}{\partial t} = -\nabla\mathbf{q}\,. \tag{A.13}$$

Using various concepts and definitions from Biot theory,

$$\sigma = \sigma' + \alpha p, \tag{A.14}$$

$$\sigma' = -\frac{\varepsilon}{C_m}, \tag{A.15}$$

$$\alpha = 1 - \frac{C_s}{C_m}, \tag{A.16}$$

one can eliminate the isotropic total stress from (A.13) to find

$$\frac{\partial\varepsilon}{\partial t} + \phi\left(C_g - C_s\right)\frac{\partial p}{\partial t} + \alpha C_s\frac{\partial p}{\partial t} - \frac{C_s}{C_m}\frac{\partial\varepsilon}{\partial t} = -\nabla\mathbf{q}. \tag{A.17}$$

Grouping of terms gives the storage equation:

$$\alpha\frac{\partial\varepsilon}{\partial t} + S\frac{\partial p}{\partial t} = \nabla\left(\frac{k}{\mu}\nabla p\right), \tag{A.18}$$

with the storativity coefficient S defined as

$$S = \phi C_g + (\alpha - \phi) C_s \, . \tag{A.19}$$

A.2 Flow problem transformation to pseudopressure

The basic governing equation is the fluid mass balance:

$$\frac{\partial\left(\phi\rho_{\mathrm{g}}\right)}{\partial t}+\nabla\left(\rho_{\mathrm{g}}\phi\mathbf{v}_{\mathrm{g}}\right)=0\,. \tag{A.20}$$

Using Darcy's law and the real gas equation of state, one can express both flow velocity and gas density in terms of pressure:

$$\phi\mathbf{v}_{\mathrm{g}}=-\frac{k}{\mu}\nabla p\,, \tag{A.21}$$

$$\rho_{\mathrm{g}}=\frac{pM}{ZRT}\,. \tag{A.22}$$

Substitution in (A.20) assuming constant porosity and isothermal conditions, one obtains:

$$\phi\frac{\partial}{\partial t}\left(\frac{p}{Z}\right)-\nabla\left(\frac{k}{\mu}\frac{p}{Z}\nabla p\right)=0\,. \tag{A.23}$$

Introduce the real gas pseudopressure $m(p)$, defined as

$$m(p)=2\int_{p_{\mathrm{ref}}}^{p}\frac{k}{\mu(p)}\frac{p}{Z(p)}\,\mathrm{d}p\,, \tag{A.24}$$

noting the pressure dependence of gas viscosity and real gas deviation factor. It is possible to rewrite (A.23) in terms of m. Firstly, the operand of the divergence term can be expressed in terms of m:

$$\frac{1}{2}\nabla m=\frac{1}{2}\frac{\partial m}{\partial p}\nabla p=\frac{k}{\mu}\frac{p}{Z}\nabla p\,. \tag{A.25}$$

For the other half of (A.23), first remove the gas deviation factor from the temporal derivative:

$$\frac{\partial}{\partial t}\left(\frac{p}{Z}\right)=\frac{\partial}{\partial t}\left(\rho_{\mathrm{g}}\frac{RT}{M}\right)=\frac{RT}{M}\frac{\partial\rho_{\mathrm{g}}}{\partial p}\frac{\partial p}{\partial t}=\rho_{\mathrm{g}}C_{\mathrm{g}}\frac{RT}{M}\frac{\partial p}{\partial t}=C_{\mathrm{g}}\frac{p}{Z}\frac{\partial p}{\partial t}\,. \tag{A.26}$$

Differentiation of m with respect to time gives

$$\frac{\partial m}{\partial t}=\frac{\partial m}{\partial p}\frac{\partial p}{\partial t}=2\frac{k}{\mu}\frac{p}{Z}\frac{\partial p}{\partial t}\,, \tag{A.27}$$

and after isolating the pressure derivative one obtains:

$$\frac{\partial p}{\partial t}=\frac{1}{2}\frac{\mu}{k}\frac{Z}{p}\frac{\partial m}{\partial t}\,. \tag{A.28}$$

Finally, upon substitution of (A.28) in (A.26) and inserting its result in (A.23) along with (A.25), one obtains a differential equation in terms of m [*Al-Hussainy et al.*, 1966]:

$$\frac{\phi\mu(p)C_{\mathrm{g}}(p)}{k}\frac{\partial m}{\partial t} - \nabla^2 m = 0\,. \tag{A.29}$$

It should be noted that this equation is still nonlinear due to the pressure dependence of the gas viscosity μ and the isothermal compressibility C_{g}.

A.3 Elastic problem

The equations of motion reduce to equations of equilibrium when the second derivative of the displacement vector **u** with respect to time (the change in momentum) is assumed to be negligible.

$$\boldsymbol{\nabla} \cdot \boldsymbol{\sigma} - \mathbf{f} = \mathbf{0}, \tag{A.30}$$

where $\boldsymbol{\sigma}$ is the second order Cauchy stress tensor (note the sign convention for soil mechanics) and **f** represents the body forces in all coordinate directions, if present. Additionally, the problem must satisfy the strain-displacement relations (or compatibility equations):

$$\boldsymbol{\varepsilon} = \frac{1}{2}\left[\boldsymbol{\nabla}\mathbf{u} + (\boldsymbol{\nabla}\mathbf{u})^T\right], \tag{A.31}$$

where $\boldsymbol{\varepsilon}$ is the infinitesimal strain tensor. Lastly, stress and strain are linearly related via Hooke's law in the constitutive relations:

$$\boldsymbol{\sigma} = \mathbf{C} : \boldsymbol{\varepsilon}, \tag{A.32}$$

where **C** is a fourth-order stiffness tensor. For a three-dimensional isotropic material, this amounts to 21 equations in total (6 equilibrium equations, 9 strain-displacement relations and 6 independent constitutive equations), one for each of the unknowns (3 displacements, 9 stresses and 9 strains).

Rewriting (A.30) for an axially symmetric cylindrical coordinate system in the absence of body forces, one obtains two equations of equilibrium:

$$\frac{\partial \sigma_{rr}}{\partial r} + \frac{\sigma_{rr} - \sigma_{tt}}{r} + \frac{\partial \sigma_{zr}}{\partial z} = 0, \tag{A.33}$$

$$\frac{\partial \sigma_{rz}}{\partial r} + \frac{\sigma_{rz}}{r} + \frac{\partial \sigma_{zz}}{\partial z} = 0. \tag{A.34}$$

Additionally, the moments applied by shear stresses must balance, requiring symmetry in the shear stress components:

$$\sigma_{rz} = \sigma_{zr}. \tag{A.35}$$

The compatibility equations, which mathematically prohibit gaps or overlapping volumes in the solution, allow the strain components to be expressed in terms of solid displacements. Due to the symmetry of the problem, all tangential derivatives must vanish, giving rise to the following four expressions for the components of strain:

$$\varepsilon_{rr} = \frac{\partial u_r}{\partial r}\,, \tag{A.36}$$

$$\varepsilon_{\theta\theta} = \frac{u_r}{r}\,, \tag{A.37}$$

$$\varepsilon_{zz} = \frac{\partial u_z}{\partial z}\,, \tag{A.38}$$

$$\varepsilon_{rz} = \varepsilon_{zr} = \frac{1}{2}\left(\frac{\partial u_r}{\partial z} + \frac{\partial u_z}{\partial r}\right). \tag{A.39}$$

The linear relation between strain and effective stress expressed in (A.32) is simplified considerably for an isotropic material, expanding into four stress-strain relations:

$$\sigma'_{rr} = -\left(K - \tfrac{2}{3}G\right)\varepsilon - 2G\varepsilon_{rr}\,, \tag{A.40}$$

$$\sigma'_{\theta\theta} = -\left(K - \tfrac{2}{3}G\right)\varepsilon - 2G\varepsilon_{\theta\theta}\,, \tag{A.41}$$

$$\sigma'_{zz} = -\left(K - \tfrac{2}{3}G\right)\varepsilon - 2G\varepsilon_{zz}\,, \tag{A.42}$$

$$\sigma'_{rz} = -2G\varepsilon_{rz}\,. \tag{A.43}$$

Substituting the compatibility equations (A.36-39) in the constitutive equations (A.40-43) and making use of Terzaghi's principle of effective stress, the total stresses can be expressed in terms of solid displacements and pore pressure:

$$\sigma_{rr} = -\left(K + \tfrac{4}{3}G\right)\frac{\partial u_r}{\partial r} - \left(K - \tfrac{2}{3}G\right)\left(\frac{u_r}{r} + \frac{\partial u_z}{\partial z}\right) + \alpha p, \tag{A.44}$$

$$\sigma_{\theta\theta} = -\left(K + \tfrac{4}{3}G\right)\frac{u_r}{r} - \left(K - \tfrac{2}{3}G\right)\left(\frac{\partial u_r}{\partial r} + \frac{\partial u_z}{\partial z}\right) + \alpha p, \tag{A.45}$$

$$\sigma_{zz} = -\left(K + \tfrac{4}{3}G\right)\frac{\partial u_z}{\partial z} - \left(K - \tfrac{2}{3}G\right)\left(\frac{\partial u_r}{\partial r} + \frac{u_r}{r}\right) + \alpha p, \tag{A.46}$$

$$\sigma_{rz} = -G\frac{\partial u_r}{\partial z} - G\frac{\partial u_z}{\partial r}\,. \tag{A.47}$$

Using (A.44-47) to rewrite the equations of equilibrium in terms of displacements and fluid pressure enables numerical solution of the mechanical problem, after which the same relations can be used to determine the (approximate) state of stress at any location in the domain.

A.4 Stress field coordinate transformation

From the point of view of a regular Cartesian coordinate system, the reference frame of the computed stress state at a given location in the reservoir is rotated about the z-axis at an angle θ, as given by its radial coordinates. The target reference frame is, from the point of view of a regular Cartesian coordinate system, rotated about the y-axis at an angle φ: the angle of the investigated plane relative to the vertical.

Let the original reference frame be denoted k_1, k_2, k_3 and the target reference frame be denoted $\hat{k}_1$, $\hat{k}_2$, $\hat{k}_3$. To compute the complete set of direction cosines, find the base vectors of both reference frames:

$$\mathbf{e_1} = \begin{bmatrix} \cos\theta \\ \sin\theta \\ 0 \end{bmatrix}, \quad \mathbf{e_2} = \begin{bmatrix} -\sin\theta \\ \cos\theta \\ 0 \end{bmatrix}, \quad \mathbf{e_3} = \begin{bmatrix} 0 \\ 0 \\ 1 \end{bmatrix}, \tag{A.48}$$

$$\hat{\mathbf{e}}_\mathbf{1} = \begin{bmatrix} \cos\varphi \\ 0 \\ \sin\varphi \end{bmatrix}, \quad \hat{\mathbf{e}}_\mathbf{2} = \begin{bmatrix} 0 \\ 1 \\ 0 \end{bmatrix}, \quad \hat{\mathbf{e}}_\mathbf{3} = \begin{bmatrix} -\sin\varphi \\ 0 \\ \cos\varphi \end{bmatrix}. \tag{A.49}$$

As the inner product of two unit vectors is equal to the cosine of the angle between them, the full set of direction cosines that combine to form the transformation matrix is given by

$$\mathbf{D}(\theta, \varphi) = \left[\mathbf{e_1}\ \mathbf{e_2}\ \mathbf{e_3}\right]^T \cdot \left[\hat{\mathbf{e}}_\mathbf{1}\ \hat{\mathbf{e}}_\mathbf{2}\ \hat{\mathbf{e}}_\mathbf{3}\right], \tag{A.50}$$

after which transformation of the stress tensor is achieved via

$$\hat{\boldsymbol{\sigma}} = \mathbf{D} \cdot \boldsymbol{\sigma} \cdot \mathbf{D}^T. \tag{A.51}$$

A.5 Seismic model

The seismic model used to evaluate the computed stress fields in terms of their triggering potential is derived from the model put forward by *Dieterich* [1994], in which an equation in terms of one or more state variables describes a population of earthquake nucleation sources, all moving towards instability. Given a certain stressing history and the initial condition of the system, the rate of earthquake production can be predicted. Key aspect of the model is that not just the state but also the rate of stress determines the amount of seismic activity, such that if the stress field is not perturbed there exists a constant rate of earthquake nucleation.

Segall and Lu [2015] put forward a way of rewriting the state variable description to obtain a single differential equation for the rate of earthquake nucleation relative to the background rate, eliminating the state variable. The model is written in terms of the Coulomb stressing rate $\dot{\tau}_c$, with the Coulomb stress defined as $\tau_c = \tau_s + \mu\sigma_n$. (Mind the fact that the sign convention used by the authors is not the one used in soil mechanics.) A constitutive parameter A, an ambient effective normal stress $\bar{\sigma}_n$ and a background Coulomb stressing rate $\dot{\tau}_{c,0}$ make up the distinguishing constants.

A.5.1 From Dieterich to Segall & Lu

Elimination of the state variable $\gamma(t)$ is achieved as follows. Starting from two equations in the original paper by Dieterich, the first of which expresses the relative seismicity rate $R(t)$ in terms of γ and $\dot{\tau}_{c,0}$:

$$R(t) = \frac{1}{\gamma(t) \cdot \dot{\tau}_{c,0}} \,. \tag{A.52}$$

The second is an expression for the state variable differential $\mathrm{d}\gamma$:

$$\mathrm{d}\gamma = \frac{1}{A\bar{\sigma}_n} \left[\mathrm{d}t - \gamma \cdot \mathrm{d}\tau_c\right] \,. \tag{A.53}$$

The Coulomb stress differential in (A.53) is expanded to a time differential,

$$\mathrm{d}\tau_c = \frac{\mathrm{d}\tau_c}{\mathrm{d}t}\,\mathrm{d}t = \dot{\tau}_c \cdot \mathrm{d}t \,, \tag{A.54}$$

after which it can be moved to the left-hand side to obtain an expression for the derivative of the state variable γ with respect to time:

$$\frac{\mathrm{d}\gamma}{\mathrm{d}t} = \frac{1}{A\bar{\sigma}_n} \left[1 - \gamma\dot{\tau}_c\right] \,. \tag{A.55}$$

Rearranging (A.52) to isolate the state variable gives the following expression for γ:

$$\gamma(t) = \frac{1}{R\dot{\tau}_{c,0}} \,, \tag{A.56}$$

which can be substituted in (A.55) to obtain a way of expressing the time derivative of γ in terms of the other variables,

$$\frac{\mathrm{d}\gamma}{\mathrm{d}t} = \frac{1}{A\bar{\sigma}_n} \left[1 - \frac{\dot{\tau}_c}{R\dot{\tau}_{c,0}}\right] \,. \tag{A.57}$$

Differentiating (A.52) with respect to time, leaving γ in the denominator and applying the chain rule, one finds:

$$\frac{\mathrm{d}R}{\mathrm{d}t} = \frac{1}{\dot{\tau}_{\mathrm{c},0}} \cdot \frac{\mathrm{d}}{\mathrm{d}t}\left(\frac{1}{\gamma}\right) = \frac{1}{\dot{\tau}_{\mathrm{c},0}}\left(-\frac{1}{\gamma^2}\frac{\mathrm{d}\gamma}{\mathrm{d}t}\right) , \tag{A.58}$$

upon which substitution of expressions (A.56) and (A.57) eliminates the state variable, leaving

$$\frac{\mathrm{d}R}{\mathrm{d}t} = -\frac{1}{\dot{\tau}_{\mathrm{c},0}} \cdot R^2 \dot{\tau}_{\mathrm{c},0}^2 \frac{1}{A\bar{\sigma}_{\mathrm{n}}}\left[1 - \frac{\dot{\tau}_{\mathrm{c}}}{R\dot{\tau}_{\mathrm{c},0}}\right] . \tag{A.59}$$

As a last step, define a characteristic time scale (A.60),

$$t_{\mathrm{a}} \equiv \frac{A\bar{\sigma}}{\dot{\tau}_{\mathrm{c},0}} , \tag{A.60}$$

after which substitution and rearrangement leaves the expression put forward by *Segall and Lu* [2015]:

$$\frac{\mathrm{d}R}{\mathrm{d}t} = \frac{R}{t_{\mathrm{a}}}\left[\frac{\dot{\tau}_{\mathrm{c}}}{\dot{\tau}_{\mathrm{c},0}} - R\right] . \tag{A.61}$$

A.5.2 Solution for R

Expanding the brackets to group terms of R and R^2 gives:

$$\frac{\mathrm{d}R}{\mathrm{d}t} = \frac{1}{t_{\mathrm{a}}}\frac{\dot{\tau}_{\mathrm{c}}}{\dot{\tau}_{\mathrm{c},0}} \cdot R - \frac{1}{t_{\mathrm{a}}} \cdot R^2 . \tag{A.62}$$

Using the chain rule and a new variable defined as $\nu \equiv R^{-1}$, one finds the following expression for de derivative of ν with respect to time:

$$\frac{\mathrm{d}\nu}{\mathrm{d}t} = -R^{-2} \cdot \frac{\mathrm{d}R}{\mathrm{d}t} , \tag{A.63}$$

in which (A.62) is substituted in its entirety, along with a sign reversal, to obtain

$$R^{-2} \cdot \frac{\mathrm{d}R}{\mathrm{d}t} = \frac{1}{t_{\mathrm{a}}}\frac{\dot{\tau}_{\mathrm{c}}}{\dot{\tau}_{\mathrm{c},0}} \cdot R^{-1} - \frac{1}{t_{\mathrm{a}}} \tag{A.64}$$

$$= \frac{1}{t_{\mathrm{a}}}\frac{\dot{\tau}_{\mathrm{c}}}{\dot{\tau}_{\mathrm{c},0}} \cdot \nu - \frac{1}{t_{\mathrm{a}}} . \tag{A.65}$$

This leaves a differential equation for ν which is both linear and first order:

$$\frac{\mathrm{d}\nu}{\mathrm{d}t} = -\left[\frac{1}{t_{\mathrm{a}}}\frac{\dot{\tau}_{\mathrm{c}}}{\dot{\tau}_{\mathrm{c},0}} \cdot \nu - \frac{1}{t_{\mathrm{a}}}\right] . \tag{A.66}$$

Define two coefficients for clarity,

$$k \equiv \frac{1}{t_\mathrm{a}}\,, \qquad P(t) \equiv \frac{1}{t_\mathrm{a}} \frac{\dot{\tau}_\mathrm{c}}{\dot{\tau}_{\mathrm{c},0}}\,, \tag{A.67}$$

substitution of which shows the characteristic form of a linear first order ODE:

$$\frac{\mathrm{d}\nu}{\mathrm{d}t} = k - P(t) \cdot \nu\,. \tag{A.68}$$

This differential equation (A.68) can be solved using the integrating factor

$$M(t) = \exp\left[\int_0^t P(s)\,\mathrm{d}s\right], \tag{A.69}$$

by which (A.68) is multiplied to give

$$M(t) \cdot \frac{\mathrm{d}\nu}{\mathrm{d}t} = M(t) \cdot k - M(t) \cdot P(t) \cdot \nu\,. \tag{A.70}$$

Bringing the multiple of ν to the left-hand side, one can apply the product rule in reverse to obtain

$$M(t) \cdot \frac{\mathrm{d}\nu}{\mathrm{d}t} + M(t) \cdot P(t) \cdot \nu = M(t) \cdot k = \frac{\mathrm{d}}{\mathrm{d}t}\left(M(t) \cdot \nu\right), \tag{A.71}$$

which is subsequently integrated to find

$$\int_0^t M(x) \cdot k\,\mathrm{d}x + C = M(t) \cdot \nu\,. \tag{A.72}$$

Finally, isolating ν and writing the integrating factor $M(t)$ in full gives the following solution:

$$\nu = \frac{\displaystyle\int_0^t k \exp\left[\int_0^x P(s)\,\mathrm{d}s\right]\mathrm{d}x + C}{\displaystyle\exp\left[\int_0^t P(s)\,\mathrm{d}s\right]}\,. \tag{A.73}$$

The constraint that $\lim_{t\to 0}\left[R(t)\right] = 1$ requires that $C = 1$, after which the fact that by definition $R = \nu^{-1}$ gives the solution for R:

$$R = \frac{\displaystyle\exp\left[\frac{1}{t_\mathrm{a}\dot{\tau}_{\mathrm{c},0}} \cdot \tau_{\mathrm{c,incr}}\right]}{\displaystyle\frac{1}{t_\mathrm{a}}\int_0^t \exp\left[\frac{1}{t_\mathrm{a}\dot{\tau}_{\mathrm{c},0}} \cdot \tau_{\mathrm{c,incr}}\right]\mathrm{d}x + 1} \tag{A.74}$$

B: Discretisation

Numerical modeling was performed in Matlab, in which a sequential finite volume/finite element routine was developed to solve the discrete problem in radial coordinates with fluid pressure p and solid displacements u_r and u_z as primary unknowns. Using the obtained displacement solution, the resultant stress field can be computed using Hooke's law (A.32) and the compatibility equations (A.31).

B.1 Fluid flow

Starting from the diffusion equation in terms of pseudopressure, noting that gas viscosity μ and isothermal compressibility C_g are functions of p:

$$\frac{\phi\mu C_\mathrm{g}}{k}\frac{\partial m}{\partial t} - \nabla^2 m = 0, \tag{B.1}$$

expanding the Laplacian for cylindrical coordinates gives

$$\frac{\phi\mu C_\mathrm{g}}{k}\frac{\partial m}{\partial t} = \frac{1}{r}\frac{\partial}{\partial r}\left(r\frac{\partial m}{\partial r}\right) + \frac{\partial}{\partial z}\left(\frac{\partial m}{\partial z}\right). \tag{B.2}$$

Integrating over a radially symmetric volume element, approximated as $\mathrm{d}V = 2\pi r \mathrm{d}A$, one obtains

$$\int_A \frac{\phi\mu C_\mathrm{g}}{k}\frac{\partial m}{\partial t}\, 2\pi r \,\mathrm{d}A = \int_A \frac{1}{r}\frac{\partial}{\partial r}\left(r\frac{\partial m}{\partial r}\right) 2\pi r \,\mathrm{d}A + \int_A \frac{\partial}{\partial z}\left(\frac{\partial m}{\partial z}\right) 2\pi r \,\mathrm{d}A, \tag{B.3}$$

in which the right-hand side can be rewritten using the divergence theorem to find

$$\int_A \frac{\phi\mu C_\mathrm{g}}{k}\frac{\partial m}{\partial t}\, 2\pi r \,\mathrm{d}A = \int_S \Big(2\pi r \nabla m \cdot \mathbf{n}\Big)\,\mathrm{d}S. \tag{B.4}$$

Discretisation in time is achieved using backward differences;

$$\int_A \left\{\frac{\phi\mu C_\mathrm{g}}{k}\right\}^{n+1} \cdot \frac{m^{n+1} - m^n}{\Delta t}\, 2\pi r \,\mathrm{d}A = \int_S \Big(2\pi r \nabla m \cdot \mathbf{n}\Big)\,\mathrm{d}S, \tag{B.5}$$

after which the problem is discretised in space with the finite volume method, making use of a two-point flux approximation scheme taken from *Karimi-Fard et al.* [2003]. This results in the following expression for every cell k:

$$\left\{\frac{\phi\mu C_\mathrm{g}}{k}\right\}_k^{n+1} \cdot \frac{m_k^{n+1} - m_k^n}{\Delta t}\, 2\pi r_{\mathrm{c},k} A_k = \sum_{\lambda=1}^{n_\lambda} \left[2\pi r_{\mathrm{c,f}} L_\mathrm{f}\, \nabla m\Big|_\mathrm{f} \cdot \mathbf{n}_\mathrm{f}\right] \tag{B.6}$$

$$= \sum_{\lambda=1}^{n_\lambda} \Big[T_{k\lambda}(m_\lambda - m_k)\Big], \tag{B.7}$$

where n_λ is the number of neighbouring cells, the subscript f denotes the face shared between a pair of cells and r_c is the radial coordinate at the centroid of a cell or interface.

Note that both fluid viscosity μ and compressibility C_f are functions of pressure p. Transmissibility between cell k and neighbour λ is computed as the harmonic average of each cell's half-transmissibility:

$$T_{k\lambda} = \frac{\alpha_k \alpha_\lambda}{\alpha_k + \alpha_\lambda}\,, \qquad \alpha_i = \frac{A_\mathrm{f}}{D_i}\mathbf{n}_i \cdot \mathbf{f}_i\,, \tag{B.8}$$

with D_i the distance between the cell and interface centroids, $\mathbf{f}_i$ the unit vector pointing inwards along that path and $\mathbf{n}_i$ the unit inward normal to the interface. Rewriting to form terms dependent on each of the pseudopressure unknowns gives a nonlinear system of $n_{e,\mathrm{pr}}$ equations of the following form:

$$\Big(\mathbf{A}\Delta t + \mathbf{B}(p)\Big) \cdot \mathbf{m}^{n+1} = \mathbf{B}(p) \cdot \mathbf{m}^{n} + \mathbf{q}, \tag{B.9}$$

with the superscript indicating the time step. Due to the pressure dependence of matrix $\mathbf{B}$, (B.9) requires an iterative solution method. Picard iteration was found to provide sufficient computational efficiency.

B.2 Mechanics

Discretisation of the mechanical problem is adapted from *Verruijt* [2016], with the novel implementation of pore pressure as a body force taken from a previously computed pseudopressure.

B.2.1 Equations & unknowns

The mechanical problem is governed by two equilibrium equations:

$$\frac{\partial \sigma_{rr}}{\partial r} + \frac{\sigma_{rr} - \sigma_{tt}}{r} + \frac{\partial \sigma_{zr}}{\partial z} = 0\,, \tag{B.10}$$

$$\frac{\partial \sigma_{rz}}{\partial r} + \frac{\sigma_{rz}}{r} + \frac{\partial \sigma_{zz}}{\partial z} = 0\,. \tag{B.11}$$

The unknowns that constitute the solution of the two-dimensional problem are the solid displacements u_r and u_z.

B.2.2 Boundary conditions

Every point on the domain boundary $\partial\Omega$ requires two boundary conditions, one for each of the two governing equations. Either a displacement (Dirichlet condition) or surface traction (Neumann condition) is specified:

$$\begin{aligned} \partial\Omega_{u_r,\mathrm{D}} &: u_r &&= a\,, \\ \partial\Omega_{u_r,\mathrm{N}} &: \sigma_{nr} &&= \sigma_{rr} n_r + \sigma_{zr} n_z = -t_r\,; \end{aligned} \tag{B.12}$$

$$\begin{aligned} \partial\Omega_{u_z,\mathrm{D}} &: u_z &&= b\,, \\ \partial\Omega_{u_z,\mathrm{N}} &: \sigma_{nz} &&= \sigma_{zz} n_z + \sigma_{rz} n_r = -t_z\,, \end{aligned} \tag{B.13}$$

with the two subsets of $\partial\Omega$ combining to form the entire domain boundary in both (B.12) and (B.13).

B.2.3 Spatial discretisation

The problem is discretised in space using the finite element method, with the discrete unknowns $u_{r,i}$ and $u_{z,i}$ located at cell vertices. By weighted summation using linear basis functions, both the global geometric coordinates (B.14) and the continuous displacement field (B.15) can be interpolated from their discrete counterparts:

$$r = \sum_{i=1}^{n_\mathrm{n}} N_i r_i, \qquad z = \sum_{i=1}^{n_\mathrm{n}} N_i z_i\,, \tag{B.14}$$

$$u_r = \sum_{i=1}^{n_\mathrm{n}} N_i u_{r,i}, \qquad u_z = \sum_{i=1}^{n_\mathrm{n}} N_i u_{z,i}\,. \tag{B.15}$$

The governing equations can be solved in terms of these interpolated variables using the Galerkin method of weighted residuals, in which the equations are rewritten in the form of

a linear system which forces equilibrium to hold on the spatial average using the n_n basis functions as weights.

As the values of the basis functions and their spatial derivatives are known across the domain and the other variables can be expressed in terms of the two unknown displacements using constitutive relations and definitions, each governing equation provides n_n equations for n_n unknown displacements. These equations must hold for all nodes, except those for which its corresponding unknown is prescribed as a Dirichlet boundary condition.

B.2.4 Discrete equations - Radial equilibrium

Applying the Galerkin method to the equation of horizontal equilibrium, one obtains the following expression that must be satisfied for all nodes i on which the horizontal displacement is not prescribed:

$$\iint_\Omega \left[\frac{\partial \sigma_{rr}}{\partial r} + \frac{\sigma_{rr} - \sigma_{tt}}{r} + \frac{\partial \sigma_{zr}}{\partial z} \right] N_i \; r \, \mathrm{d}r \, \mathrm{d}z = 0 \,. \tag{B.16}$$

Using the product rule of differentiation, this can be rewritten as the sum of two terms R_1 and R_2:

$$\underbrace{\iint_\Omega \left[\frac{\partial}{\partial r} \left[r \sigma_{rr} N_i \right] + \frac{\partial}{\partial z} \left[r \sigma_{zr} N_i \right] \right] \mathrm{d}r \, \mathrm{d}z}_{R_1} \underbrace{- \iint_\Omega \left[\sigma_{rr} \frac{\partial N_i}{\partial r} + \sigma_{zr} \frac{\partial N_i}{\partial z} + \sigma_{\theta\theta} \frac{\partial N_i}{r} \right] r \, \mathrm{d}r \, \mathrm{d}z}_{R_2} = 0 \,. \tag{B.17}$$

R_1 can be transformed into a known surface integral using the divergence theorem, giving

$$R_1 = \int_S \sigma_{nr} r N_i \, \mathrm{d}S, \tag{B.18}$$

and R_2 can be rewritten in terms of the discrete set of unknowns and the previously computed pressure drop Δp using the interpolators (B.15), the equations of elasticity and the various known material properties to obtain

$$\begin{aligned} R_2 = \iint_\Omega \Bigg\{ \sum_{j=1}^{n_\mathrm{n}} \Bigg[& M \left(\frac{\partial N_i}{\partial r} \frac{\partial N_j}{\partial r} + \frac{N_i}{r} \frac{N_j}{r} \right) u_{r,j} + \lambda \left(\frac{\partial N_i}{\partial r} \frac{N_j}{r} + \frac{N_i}{r} \frac{\partial N_j}{\partial r} \right) u_{r,j} \\ & + \lambda \left(\frac{\partial N_i}{\partial r} \frac{\partial N_j}{z} + \frac{N_i}{r} \frac{\partial N_j}{\partial z} \right) u_{z,j} + G \frac{\partial N_i}{\partial z} \frac{\partial N_j}{\partial z} u_{r,j} \\ & + G \frac{\partial N_i}{\partial z} \frac{\partial N_j}{\partial r} u_{z,j} \Bigg] - \alpha \left(\frac{\partial N_i}{\partial r} + \frac{N_i}{r} \right) \Delta p \Bigg\} \, r \, \mathrm{d}r \, \mathrm{d}z \,. \end{aligned} \tag{B.19}$$

Rewriting the integral over the entire domain as the sum of the integral over each element l gives:

$$R_2 = \sum_{l=1}^{n_e} \sum_{j=1}^{n_n} \left[P_{ijl} u_{r,j} + Q_{ijl} u_{z,j} \right] + \sum_{l=1}^{n_e} [S_{il} \Delta p_l], \tag{B.20}$$

where the second summation contains the effect of the pore fluid pressure drop Δp. The entries of the stiffness matrices **P**, **Q** and **S** are computed from known integrals of material properties and derivatives of basis functions, found as a set of n_e element stiffness matrices which are subsequently summed to find the stiffness matrices that make up the complete system:

$$\begin{aligned} P_{ijl} = M_l \iint_{\Omega_l} \left(\frac{\partial N_i}{\partial r} \frac{\partial N_j}{\partial r} + \frac{N_i}{r} \frac{N_j}{r} \right) r \, \mathrm{d}r \, \mathrm{d}z \\ + \lambda_l \iint_{\Omega_l} \left(\frac{\partial N_i}{\partial r} \frac{N_j}{r} + \frac{N_i}{r} \frac{\partial N_j}{\partial r} \right) r \, \mathrm{d}r \, \mathrm{d}z \\ + G_l \iint_{\Omega_l} \frac{\partial N_i}{\partial z} \frac{\partial N_j}{\partial z} \, r \, \mathrm{d}r \, \mathrm{d}z , \end{aligned} \tag{B.21}$$

$$Q_{ijl} = \lambda_l \iint_{\Omega_l} \left(\frac{\partial N_i}{\partial r} \frac{\partial N_j}{z} + \frac{N_i}{r} \frac{\partial N_j}{\partial z} \right) r \, \mathrm{d}r \, \mathrm{d}z + G_l \iint_{\Omega_l} \frac{\partial N_i}{\partial z} \frac{\partial N_j}{\partial r} \, r \, \mathrm{d}r \, \mathrm{d}z , \tag{B.22}$$

$$S_{il} = -\alpha_l \iint_{\Omega_l} \left(\frac{\partial N_i}{\partial r} + \frac{N_i}{r} \right) r \, \mathrm{d}r \, \mathrm{d}z \, . \tag{B.23}$$

B.2.5 Discrete equations - Vertical equilibrium

Applying the Galerkin method to the equation of vertical equilibrium, one obtains the following expression which must be satisfied for all nodes i on which the vertical displacement is not prescribed:

$$\iint_{\Omega} \left[\frac{\partial \sigma_{rz}}{\partial r} + \frac{\sigma_{rz}}{r} + \frac{\partial \sigma_{zz}}{\partial z} \right] N_i \; r \, \mathrm{d}r \, \mathrm{d}z = 0 \, . \tag{B.24}$$

Using the product rule of differentiation, this can be rewritten as the sum of two terms Z_1 and Z_2:

$$\underbrace{\iint_{\Omega} \left[\frac{\partial}{\partial r} [r \sigma_{rz} N_i] + \frac{\partial}{\partial z} [r \sigma_{zz} N_i] \right] \mathrm{d}r \, \mathrm{d}z}_{Z_1} \quad \underbrace{- \iint_{\Omega} \left[\sigma_{rz} \frac{\partial N_i}{\partial r} + \sigma_{zz} \frac{\partial N_i}{\partial z} \right] r \, \mathrm{d}r \, \mathrm{d}z}_{Z_2} = 0 \, . \tag{B.25}$$

Z_1 can be transformed into a known surface integral using the divergence theorem, giving

$$Z_1 = \int_S \sigma_{nz}\, r N_i \, \mathrm{d}S, \tag{B.26}$$

and Z_2 can be rewritten in terms of the discrete set of unknowns and the previously computed pressure drop Δp using the interpolators (B.15), the equations of elasticity and the various known material properties to obtain

$$Z_2 = \iint_\Omega \left\{ \sum_{j=1}^{n_\mathrm{n}} \left[M \frac{\partial N_i}{\partial z}\frac{\partial N_j}{\partial z} u_{z,j} + \lambda \left(\frac{\partial N_i}{\partial z}\frac{\partial N_j}{\partial r} + \frac{\partial N_i}{\partial z}\frac{N_j}{r} \right) u_{r,j} \right.\right. \\ \left.\left. + G \frac{\partial N_i}{\partial r}\frac{\partial N_j}{\partial r} u_{z,j} + G \frac{\partial N_i}{\partial r}\frac{\partial N_j}{\partial z} u_{r,j} \right] - \alpha \frac{\partial N_i}{\partial z} p \right\} r \, \mathrm{d}r \, \mathrm{d}z \,. \tag{B.27}$$

Rewriting the integral over the entire domain as the sum of the integral over each element l gives:

$$Z_2 = \sum_{l=1}^{n_\mathrm{e}} \sum_{j=1}^{n_\mathrm{n}} \left[Q_{jil} u_{r,j} + R_{ijl} u_{z,j} \right] + \sum_{l=1}^{n_\mathrm{e}} \left[T_{il} p_l \right], \tag{B.28}$$

where the second summation contains the effect of the known pore fluid pressure drop Δp. The entries of the stiffness matrices $\mathbf{Q}$, $\mathbf{R}$ and $\mathbf{T}$ are computed from known integrals of material properties and derivatives of basis functions, found as a set of n_e element stiffness matrices which are subsequently summed to find the stiffness matrices that make up the complete system:

$$Q_{jil} = \lambda_l \iint_{\Omega_l} \left(\frac{\partial N_i}{\partial z}\frac{\partial N_j}{\partial r} + \frac{\partial N_i}{\partial z}\frac{N_j}{r} \right) r \, \mathrm{d}r \, \mathrm{d}z + G_l \iint_{\Omega_l} \frac{\partial N_i}{\partial r}\frac{\partial N_j}{\partial z} \, r \, \mathrm{d}r \, \mathrm{d}z, \tag{B.29}$$

$$R_{ijl} = M_l \iint_{\Omega_l} \frac{\partial N_i}{\partial z}\frac{\partial N_j}{\partial z} \, r \, \mathrm{d}r \, \mathrm{d}z + G_l \iint_{\Omega_l} \frac{\partial N_i}{\partial r}\frac{\partial N_j}{\partial r} \, r \, \mathrm{d}r \, \mathrm{d}z, \tag{B.30}$$

$$T_{il} = -\alpha_l \iint_{\Omega_l} \frac{\partial N_i}{\partial z} \, r \, \mathrm{d}r \, \mathrm{d}z \,. \tag{B.31}$$

B.2.6 System of equations

Adding each element's contribution to the global stiffness matrix (using Gaussian quadratures to approximate the integrals) and moving the known constants to the right hand side, one obtains the following linear system of $2n_\mathrm{n}$ equations for $2n_\mathrm{n}$ unknowns:

$$\sum_{j=1}^{n_\mathrm{n}} P_{ij} u_{r,j} + \sum_{j=1}^{n_\mathrm{n}} Q_{ij} u_{z,j} = f_{r,i} - \sum_{l=1}^{n_\mathrm{e}} S_{il} p_l \,, \tag{B.32}$$

$$\sum_{j=1}^{n_\mathrm{n}} Q_{ji} u_{r,j} + \sum_{j=1}^{n_\mathrm{n}} R_{ij} u_{z,j} = f_{z,i} - \sum_{l=1}^{n_\mathrm{e}} T_{il} p_l \,. \tag{B.33}$$

In which the vectors $\mathbf{f}_r$ and $\mathbf{f}_z$ contain the forces applied to each node due to any prescribed surface stresses, as computed by the surface integrals (B.18) and (B.26) over the relevant boundary segments.

Although Neumann boundaries incorporate naturally, the finite element method requires the equations corresponding to Dirichlet boundary nodes to be forced to the prescribed value after system assembly by modifying both the stiffness matrix and source vector to essentially remove those degrees of freedom from the system. Details can be found in, Appendix E: Simulator algorithms.

C: Validation of finite volume solver

To validate the numerical solution of the flow problem, two verification criteria were used. Firstly, the mass of gas in the reservoir and the mass of gas produced must sum to the same amount that was initially in place. Secondly, a grid refinement study was conducted in both the spatial and temporal domain, to show consistency and stability (and thereby convergence).

C.1 Fluid mass balance

The total mass of gas produced is computed via the mass flux constraint at the wellbore, whereas the total mass of gas (initially) in place is computed by integrating the gas density over the domain.

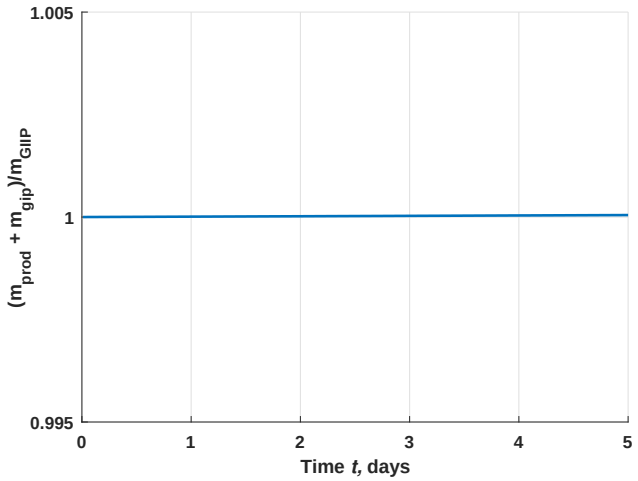

Figure C.1: Deviation from mass balance, computed as the sum of gas produced and gas remaining normalized by the initial mass of gas in place.

C.2 Grid refinement study

Grid refinement studies were conducted in both the spatial and temporal domain, showing consistency and stability of the solution method. Time step size Δt and characteristic cell size h were studied separately, with one resolution kept at the highest level so that the error caused by the resolution under investigation dominates.

C.2.1 Cell size h

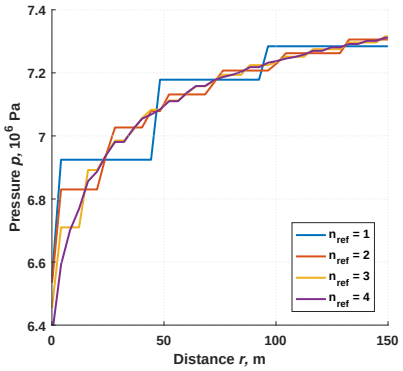

Figure C.2: Pressure at $t = 5$ days for increasing resolutions.

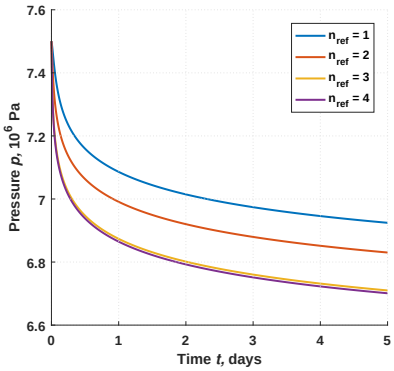

Figure C.3: Pressure at $r = 8$ m for increasing resolutions.

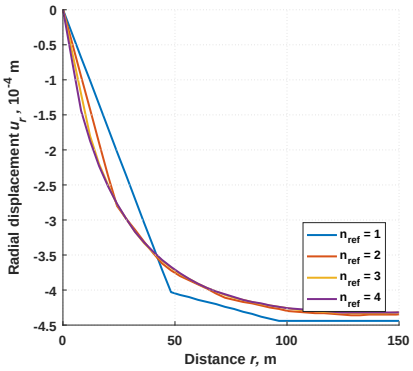

Figure C.4: Radial displacement at $t = 5$ days for increasing resolutions.

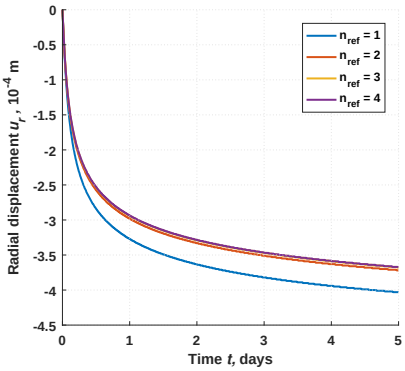

Figure C.5: Radial displacement at $r = 48$ m for increasing resolutions.

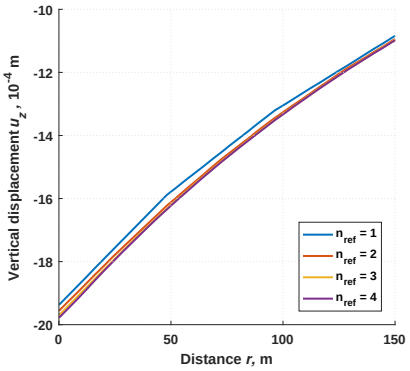

Figure C.6: Vertical displacement at $t = 5$ days for increasing resolutions, $z = H_{\text{res}}$

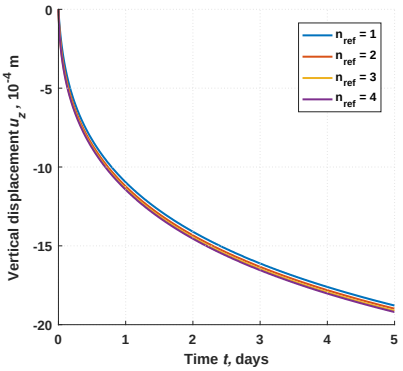

Figure C.7: Vertical displacement at $r = 8$ m for increasing resolutions, $z = H_{\text{res}}$

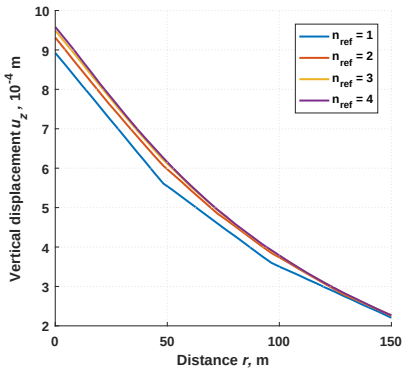

Figure C.8: Vertical displacement at $t = 5$ days for increasing resolutions, $z = 0$

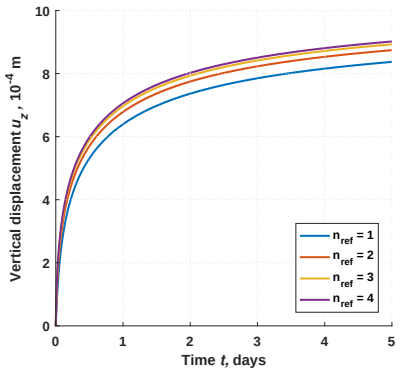

Figure C.9: Vertical displacement at $r = 8$ m for increasing resolutions, $z = 0$

C.2.2 Time step Δt

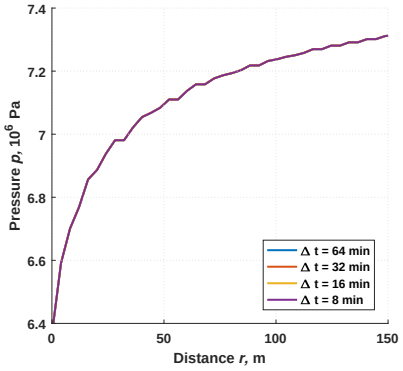

Figure C.10: Pressure at $t = 5$ days for increasing resolutions.

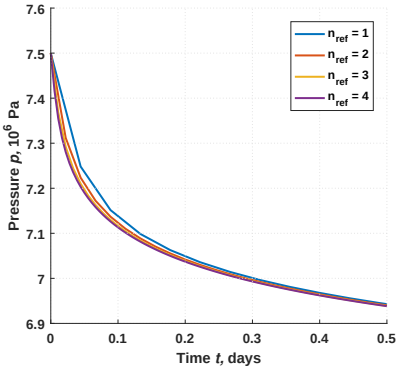

Figure C.11: Pressure at $r = 8$ m for increasing resolutions.

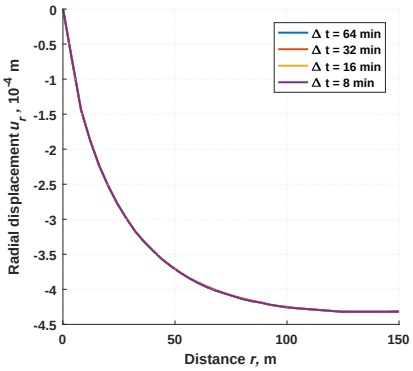

Figure C.12: Radial displacement at $t = 5$ days for increasing resolutions.

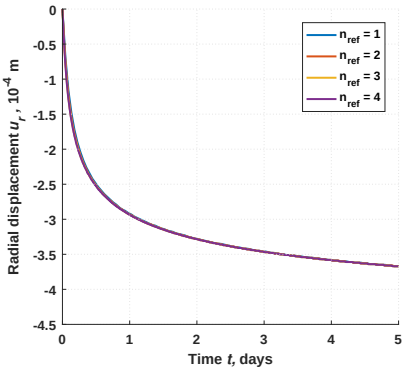

Figure C.13: Radial displacement at $r = 48$ m for increasing resolutions.

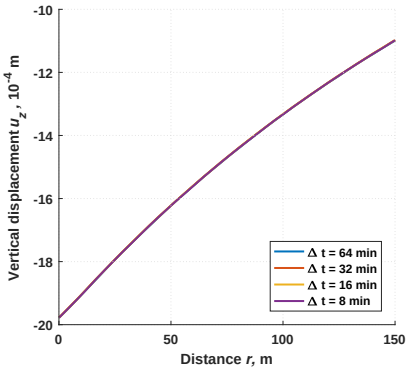

Figure C.14: Vertical displacement at $t = 5$ days for increasing resolutions, $z = H_{\text{res}}$

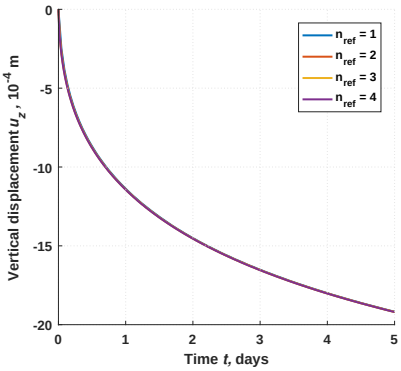

Figure C.15: Vertical displacement at $r = 8$ m for increasing resolutions, $z = H_{\text{res}}$

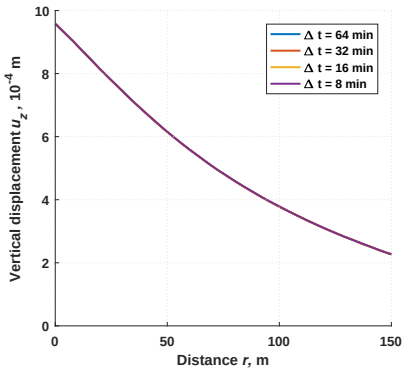

Figure C.16: Vertical displacement at $t = 5$ days for increasing resolutions, $z = 0$

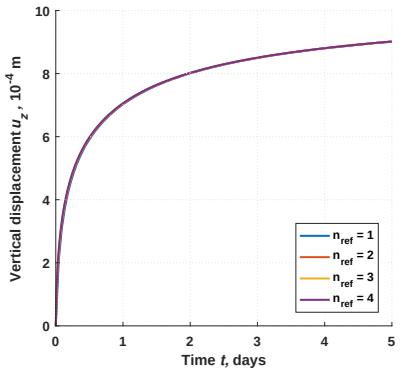

Figure C.17: Vertical displacement at $r = 8$ m for increasing resolutions, $z = 0$

D: Sensitivity study for elastic moduli

D.1 Reservoir rock

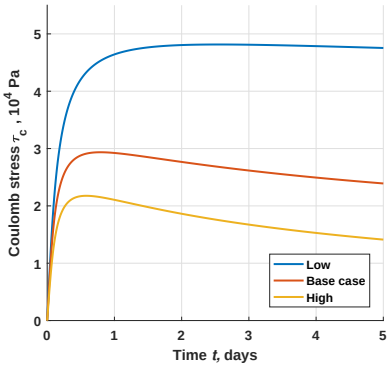

Figure D.1: Coulomb stress for high and low elastic moduli in the reservoir compared to base case.

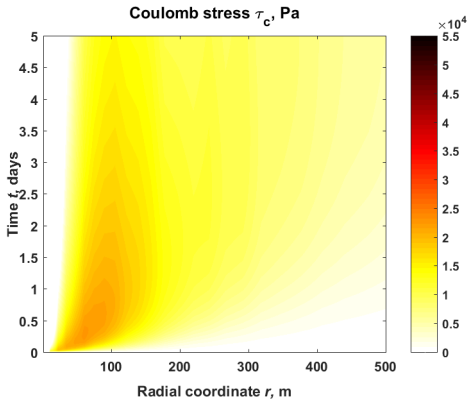

Figure D.2: Coulomb stress for high elastic moduli ($K = 2K_{\text{base}}$, $G = 2G_{\text{base}}$) in the reservoir.

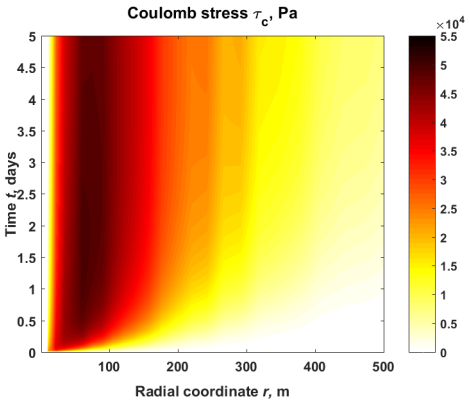

Figure D.3: Coulomb stress for low elastic moduli ($K = \frac{1}{2}K_{\text{base}}$, $G = \frac{1}{2}G_{\text{base}}$) in the reservoir.

D.2 Over- and underburden

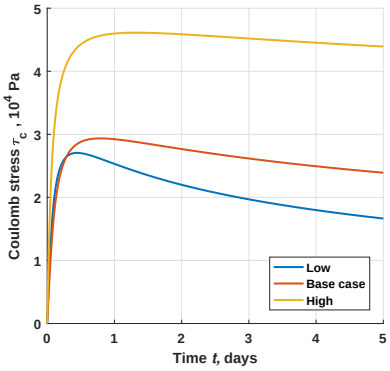

Figure D.4: Coulomb stress for high and low elastic moduli in the surrounding rock compared to base case.

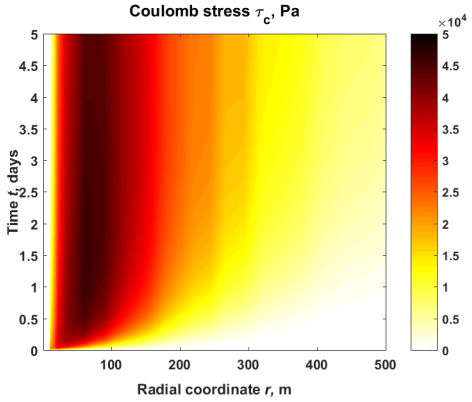

Figure D.5: Coulomb stress for high elastic moduli ($K = 2K_{\text{base}}$, $G = 2G_{\text{base}}$) in the surrounding rock.

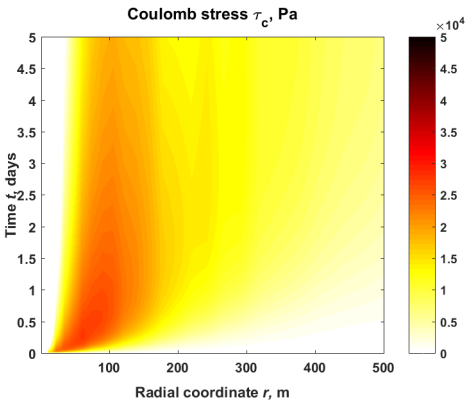

Figure D.6: Coulomb stress for low elastic moduli ($K = \frac{1}{2}K_{\text{base}}$, $G = \frac{1}{2}G_{\text{base}}$) in the surrounding rock.

E: Simulator algorithms

Algorithm Matlab reservoir simulator

INPUT
    set physical variables
    set computational parameters
PRE-PROCESSING
    compute conversion table — $[m \leftrightarrow p](..)$
    build mesh
    assign rock properties — (K, G, C_{m})
    ► *function_a* → assemble matrix components for elastic problem
        $\mathbf{P}, \mathbf{Q^1}, \mathbf{Q^2}, \mathbf{R}, \mathbf{S}, \mathbf{T}$
    ► *function_b* → assemble transmissibility matrix
        $\mathbf{A}$
INITIALIZE
    $\mathbf{p}_n \leftarrow p_{\mathrm{res},0}$
    update fluid properties
    ► *function_c* → assemble nonlinear terms $\mathbf{B}(p)$
SOLVER BODY
    for timesteps n
        $\mathbf{m}_n \leftarrow [m \leftrightarrow p](\mathbf{p}_n)$
        $\mathbf{p}^{\nu}_{n+1} \leftarrow \mathbf{p}_n$
        ► *solver_j* → nonlinear solver for $\mathbf{p}_{n+1}$
        ► *solver_k* → linear solver for $\mathbf{u}_r$, $\mathbf{u}_z$
        ► *function_d* → compute stress state
        write datafiles
        check massbalance
    end

► ***solver_j*** Nonlinear solver for pressure

while ~converged
    $\mathbf{m}^{\nu+1}_{n+1} \leftarrow (\mathbf{A} + \mathbf{B}\Delta t)\backslash(\mathbf{A}\mathbf{m}_n + \mathbf{q})$
    $\mathbf{p}^{\nu+1}_{n+1} \leftarrow [m \leftrightarrow p](\mathbf{m}^{\nu+1}_{n+1})$
    if converged
        $\mathbf{p}_{n+1} \leftarrow \mathbf{p}^{\nu}_{n+1}$
        break;
    else
        $\mathbf{p}^{\nu}_{n+1} \leftarrow \mathbf{p}^{\nu+1}_{n+1}$
        update fluid properties
        function_c → assemble nonlinear matrix $\mathbf{B}(p)$
        continue;
    end
end

▶ ***solver_k*** Linear solver for displacement

reset stiffness matrix components
% Compute body force for pore fluid pressure
$\Delta p_l \leftarrow p_{k_l} - p_{\mathrm{res},0} \quad l \in \Omega_{\mathrm{pr}}$
$\Delta p_l \leftarrow 0 \quad$ otherwise
$\mathbf{f}_r \leftarrow -(\mathbf{S}\Delta\mathbf{p})$
$\mathbf{f}_z \leftarrow -(\mathbf{T}\Delta\mathbf{p})$
% Enforce Dirichlet condition for u_r
$\mathbf{d}_r \leftarrow$ indices of nodes $i \in \partial\Omega_{u_r,\mathrm{D}}$
$\mathbf{f}_r \leftarrow \mathbf{f}_r - \mathbf{P}_{\bullet\mathbf{d}_r} \cdot \mathbf{u}_{r,D}$
$\mathbf{Q^1}_{\mathbf{d}_r\bullet} \leftarrow 0$
$\mathbf{P}_{\bullet\mathbf{d}_r} \leftarrow 0$
$\mathbf{P}_{\mathbf{d}_r\bullet} \leftarrow 0$
$\mathbf{P}_{\mathbf{d}_r\mathbf{d}_r} \leftarrow \boldsymbol{I}$
% Enforce Dirichlet condition for u_z
$\mathbf{d}_z \leftarrow$ indices of nodes $j \in \partial\Omega_{u_z,\mathrm{D}}$
$\mathbf{f}_z \leftarrow \mathbf{f}_z - \mathbf{R}_{\bullet\mathbf{d}_z} \cdot \mathbf{u}_{z,D}$
$\mathbf{Q^2}_{\mathbf{d}_z\bullet} \leftarrow 0$
$\mathbf{R}_{\bullet\mathbf{d}_z} \leftarrow 0$
$\mathbf{R}_{\mathbf{d}_z\bullet} \leftarrow 0$
$\mathbf{R}_{\mathbf{d}_z\mathbf{d}_z} \leftarrow \boldsymbol{I}$
% Assemble system and solve
$\mathbf{V} \leftarrow [\mathbf{P},\ \mathbf{Q^1}; \mathbf{Q^2},\ \mathbf{R}]$
$\mathbf{f} \leftarrow [\mathbf{f}_r; \mathbf{f}_z]$
$\mathbf{u} \leftarrow \mathbf{V}\backslash\mathbf{f}$
% Extract solution components
$\mathbf{u}_r \leftarrow$ `u(1:n_n)`
$\mathbf{u}_z \leftarrow$ `u(1+n_n:2*n_n)`

▶ ***function_a*** Matrix component assembly for mechanical problem [*Chessa*, 2002]

allocate memory for sparse matrices $\mathbf{P}$, $\mathbf{Q^1}$, $\mathbf{Q^2}$, $\mathbf{R}$, $\mathbf{S}$, $\mathbf{T}$
[`wts`, `locs`] ← Local coordinates and point weights for Gaussian quadrature
for elements l
    `ind` ← node indices for element l
    for Gauss points g
        $[\mathbf{N}, \boldsymbol{\partial}\mathbf{N}_{\text{loc}}]$ ← values of shape functions and their derivatives at Gauss point
        r_g ← `coor(1,ind)` $\cdot\, \mathbf{N}$
        $\mathbf{J_0}$ ← `coor(:,ind)` $\cdot\, \boldsymbol{\partial}\mathbf{N}_{\text{loc}}$
        $|\mathbf{J_0}|$ ← `coor(:,ind)` $\cdot\, \boldsymbol{\partial}\mathbf{N}_{\text{loc}}$
        $\boldsymbol{\partial}\mathbf{N}_{\text{glo}}$ ← $\boldsymbol{\partial}\mathbf{N}_{\text{loc}}/\mathbf{J_0}$
        $\boldsymbol{\partial r}$ ← $\boldsymbol{\partial}\mathbf{N}_{\text{glo}}$`(:,1)`
        $\boldsymbol{\partial z}$ ← $\boldsymbol{\partial}\mathbf{N}_{\text{glo}}$`(:,2)`
        % Build stiffness matrices
        $\mathbf{P}$`(ind,ind)` ← $\mathbf{P}$`(ind,ind)` $+(K_l + \frac{4}{3}G_l)\cdot(\boldsymbol{\partial r}\cdot\boldsymbol{\partial r}^T)\cdot r_{\text{g}}\ \cdot$ `wts(g)` $\cdot\,|\mathbf{J_0}|$
        $\mathbf{P}$`(ind,ind)` ← $\mathbf{P}$`(ind,ind)` $+(K_l + \frac{4}{3}G_l)\cdot(\mathbf{N}\cdot\mathbf{N}^T)\ \cdot r_{\text{g}}^{-1}\cdot$ `wts(g)` $\cdot\,|\mathbf{J_0}|$
        $\mathbf{P}$`(ind,ind)` ← $\mathbf{P}$`(ind,ind)` $+(K_l - \frac{2}{3}G_l)$ .....
        .....
        ...
        .....
        ..... $+(K_l + \frac{4}{3}G_l)\cdot(\boldsymbol{\partial z}\cdot\boldsymbol{\partial z}^T)\cdot r_{\text{g}}\ \cdot$ `wts(g)` $\cdot\,|\mathbf{J_0}|$
        $\mathbf{R}$`(ind,ind)` ← $\mathbf{R}$`(ind,ind)` $+\quad (G_l)\cdot(\boldsymbol{\partial r}\cdot\boldsymbol{\partial r}^T)\cdot r_{\text{g}}^{-1}\cdot$ `wts(g)` $\cdot\,|\mathbf{J_0}|$
        % Build matrices for pore pressure body force
        $\mathbf{S}$`(ind,1)` ← $\mathbf{S}$`(ind,1)` $-\,\alpha\cdot\boldsymbol{\partial r}\cdot r_{\text{g}}\cdot$ `wts(g)` $\cdot\,|\mathbf{J_0}|$
        $\mathbf{S}$`(ind,1)` ← $\mathbf{S}$`(ind,1)` $-\,\alpha\cdot\mathbf{N}\cdot r_{\text{g}}\cdot$ `wts(g)` $\cdot\,|\mathbf{J_0}|$
        $\mathbf{T}$`(ind,1)` ← $\mathbf{T}$`(ind,1)` $-\,\alpha\cdot\boldsymbol{\partial z}\cdot r_{\text{g}}\cdot$ `wts(g)` $\cdot\,|\mathbf{J_0}|$

▶ ***function_b*** Transmissibility matrix assembly

allocate memory for sparse matrix $\boldsymbol{A}$
for cells $l \in \Omega_{\text{pr}}$
  $k \leftarrow$ local cell index k_l
  for neighbours λ
    if $\lambda \in \Omega_{\text{pr}}$
      $\kappa \leftarrow$ local cell index κ_λ
      $\mathbf{n}_{\text{f}} \leftarrow$ unit inward normal to face $\text{f}_{k\kappa}$
      $A_{\text{f}} \leftarrow$ face area
      % Compute cell half-transmissibility
      $D_k \leftarrow$ distance from face centroid c_{f} to cell centroid c_k
      $\mathbf{f}_k \leftarrow$ unit vector pointing inwards along that path
      $\alpha_k \leftarrow (A_{\text{f}}/D_k)\,\mathbf{n}_{\text{f}} \cdot \mathbf{f}_k$
      % Compute neighbour half-transmissibility
      $D_\kappa \leftarrow$ distance from face centroid c_{f} to neighbour centroid c_κ
      $\mathbf{f}_\kappa \leftarrow$ unit vector pointing inwards along that path
      $\alpha_\kappa \leftarrow (A_{\text{f}}/D_\kappa)\,(-\mathbf{n}_{\text{f}}) \cdot \mathbf{f}_\kappa$
      % Store flow contribution
      $T_{k\kappa} \leftarrow (\alpha_k \alpha_\kappa)/(\alpha_k + \alpha_\kappa)$
      $\boldsymbol{A}(\mathtt{k},\mathtt{k}) \leftarrow \boldsymbol{A}(\mathtt{k},\mathtt{k}) + T_{k\kappa}$
      $\boldsymbol{A}(\mathtt{k},\kappa) \leftarrow \boldsymbol{A}(\mathtt{k},\kappa) - T_{k\kappa}$
    end
  end
end

▶ ***function_c*** Nonlinear matrix assembly

allocate memory for sparse matrix $\mathbf{B}$
for cells $l \in \Omega_{\text{pr}}$
  $k \leftarrow$ local cell index k_l
  $\mathbf{B}(\mathtt{k},\mathtt{k}) \leftarrow \mathbf{B}(\mathtt{k},\mathtt{k}) + (V_k \phi_l \mu_k C_{\text{g},k})/k_{\text{abs}}$
end

▶ ***function_d*** Computation of stress state from displacements (Adapted from *Chessa* [2002])

allocate memory for storage
[wts,locs] ← local coordinates and point weights for Gaussian quadrature
for elements l
    ind ← node indices for element l
    rr ← 0
    tt ← 0
    zz ← 0
    zr ← 0
    for Gauss points g
        $[\mathbf{N}, \partial\mathbf{N}_{\text{loc}}]$ ← values of shape functions and their derivatives at Gauss point
        r_g ← coor(1,ind) · $\mathbf{N}$
        $\mathbf{J_0}$ ← coor(:,ind) · $\partial\mathbf{N}_{\text{loc}}$
        $\partial\mathbf{N}_{\text{glo}}$ ← $\partial\mathbf{N}_{\text{loc}}/\mathbf{J_0}$
        $\partial\boldsymbol{r}$ ← $\partial\mathbf{N}_{\text{glo}}$(:,1)
        $\partial\boldsymbol{z}$ ← $\partial\mathbf{N}_{\text{glo}}$(:,2)
        % Take contribution from each Gauss point
        rr ← rr $+\frac{1}{3} \cdot -(K_l + \frac{4}{3}G_l) \cdot \partial\boldsymbol{r}^T \cdot \mathbf{u}_{\boldsymbol{r}}$(ind)
        rr ← rr $+\frac{1}{3} \cdot -(K_l - \frac{2}{3}G_l) \cdot \partial\boldsymbol{z}^T \cdot \mathbf{u}_{\boldsymbol{z}}$(ind)
        rr ← rr $+\frac{1}{3} \cdot -(K_l - \frac{2}{3}G_l) \cdot \mathbf{N}^T \cdot \mathbf{u}_{\boldsymbol{r}}(ind)/r_g$
        .....
        ...
        .....
        zr ← zr $+\frac{1}{3} \cdot -G_l \cdot \partial\boldsymbol{z}^T \cdot \mathbf{u}_{\boldsymbol{r}}$(ind)
        zr ← zr $+\frac{1}{3} \cdot -G_l \cdot \partial\boldsymbol{r}^T \cdot \mathbf{u}_{\boldsymbol{z}}$(ind)
    end
    store (σ')
    store $(\sigma' + \alpha \cdot \Delta p_l$
end

F: Components of stress across the reservoir at t = 1 day

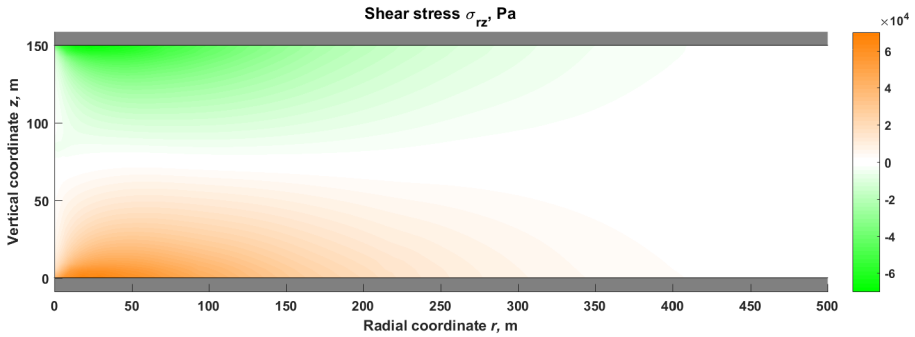

Figure F.1: *Shear stresses after 1 day of production.*

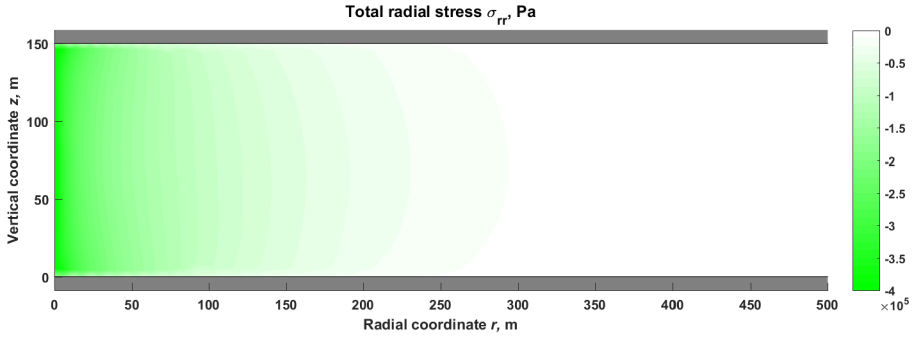

Figure F.2: *Total radial stress after 1 day of production.*

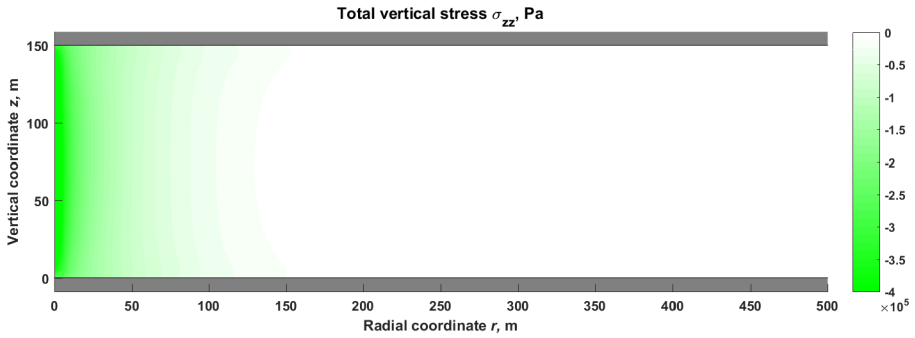

Figure F.3: *Total vertical stress after 1 day of production.*

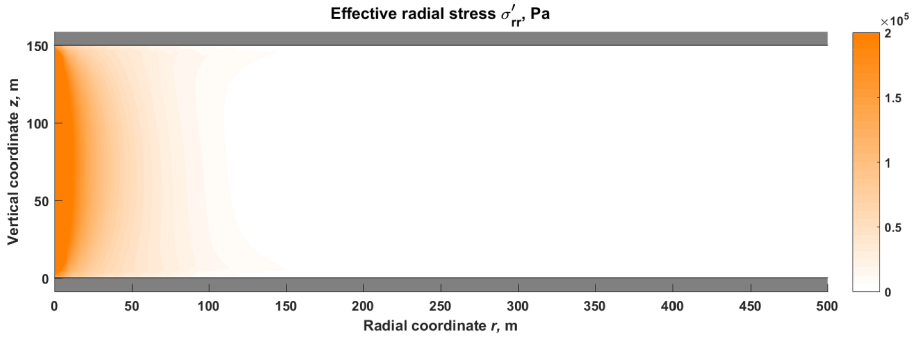

Figure F.4: *Effective radial stress after 1 day of production.*

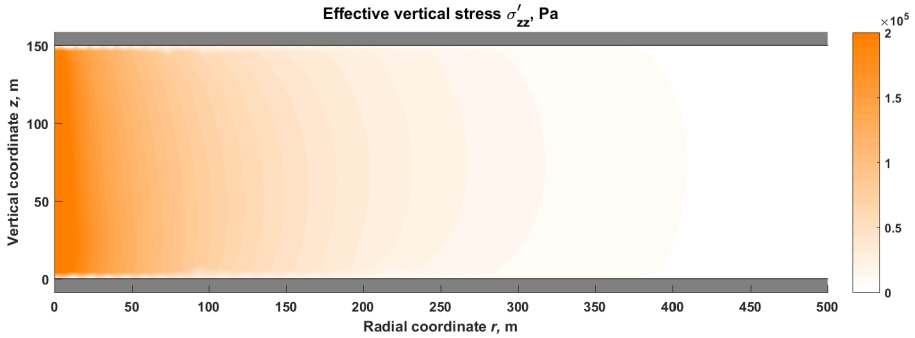

Figure F.5: *Effective vertical stress after 1 day of production.*

G: Stresses on an inclined plane after coordinate system transformation

G.1 Base case - shear and normal components

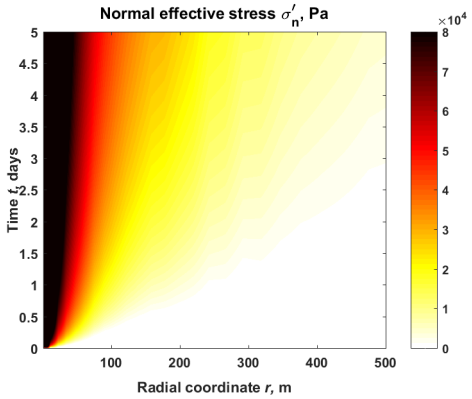

Figure G.1: Normal stress for a fault dipping towards the producer at $\theta = 85°$.

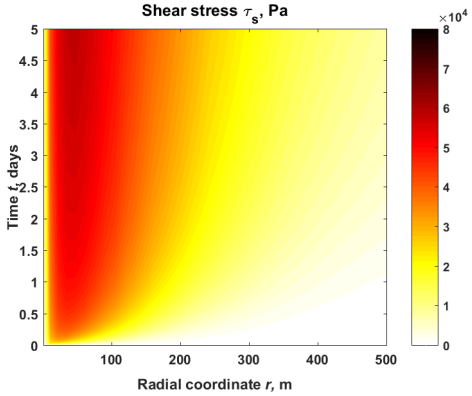

Figure G.2: Shear stress for a fault dipping towards the producer at $\theta = 85°$.

G.2 Production rate

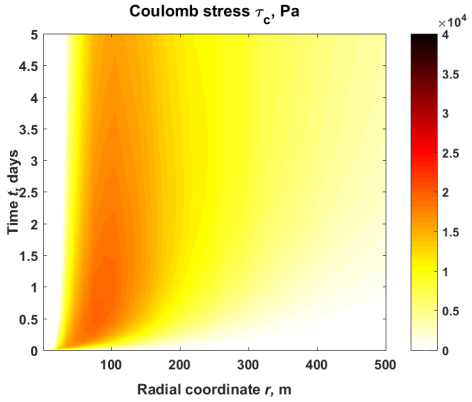

Figure G.3: Coulomb stress as a function of time and radial coordinate, $q_{sc} = 2.0 \cdot 10^6$ m^3/day.

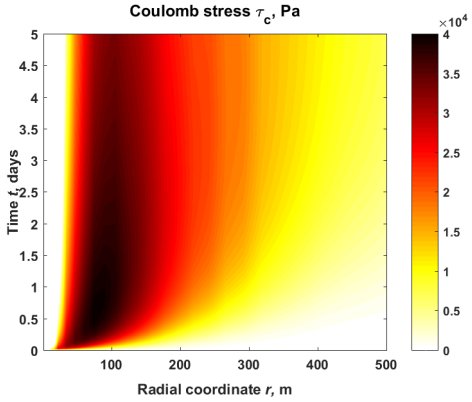

Figure G.4: Coulomb stress as a function of time and radial coordinate, $q_{sc} = 4.0 \cdot 10^6$ m^3/day.

G.3 Production ramping

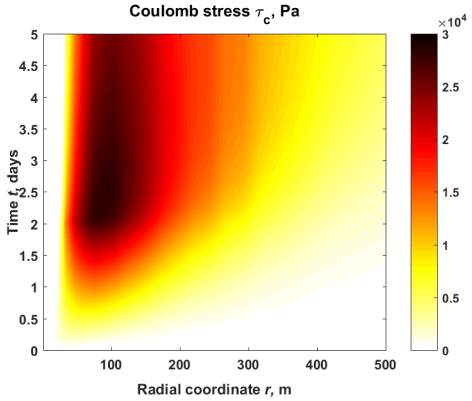

Figure G.5: Coulomb stress as a function of time and radial coordinate, $n_{\Delta q} \to \infty$.

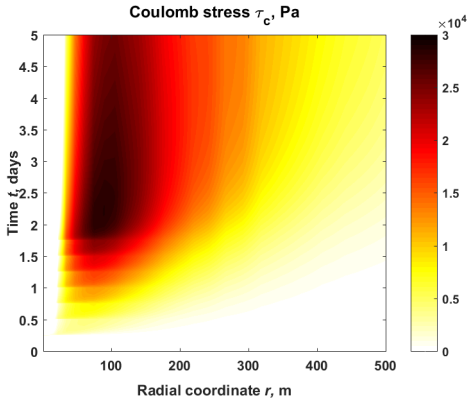

Figure G.6: Coulomb stress as a function of time and radial coordinate, $n_{\Delta q} = 7$.

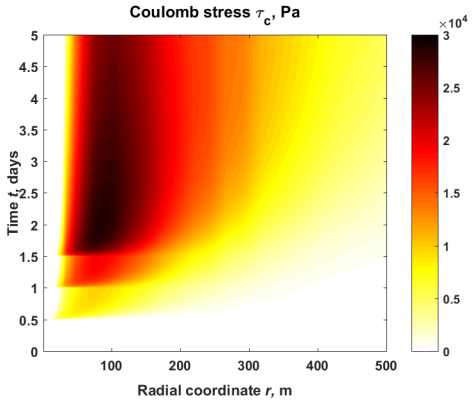

Figure G.7: Coulomb stress as a function of time and radial coordinate, $n_{\Delta q} = 3$

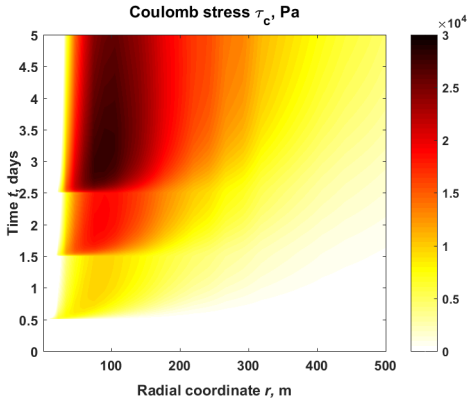

Figure G.8: Coulomb stress as a function of time and radial coordinate, $\Delta_t = 2$.

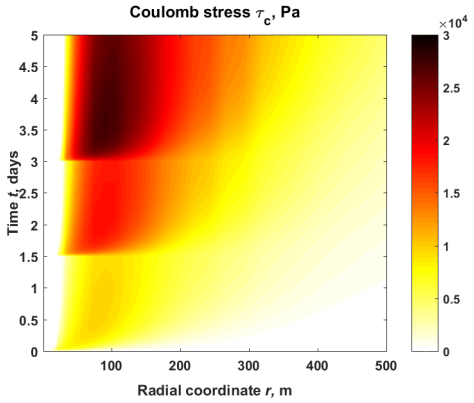

Figure G.9: Coulomb stress as a function of time and radial coordinate, $\Delta_t = 3$

G.4 Reservoir pressure

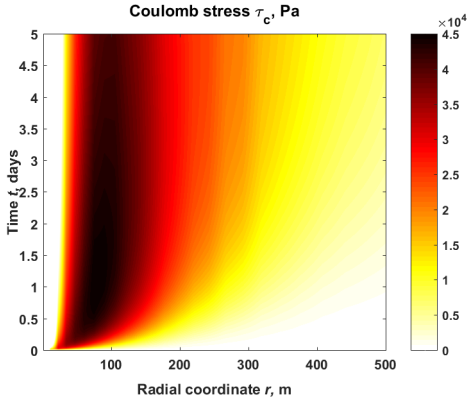

Figure G.10: Coulomb stress as a function of time and radial coordinate, $p_{\text{res},0} = 5.0 \cdot 10^6$.

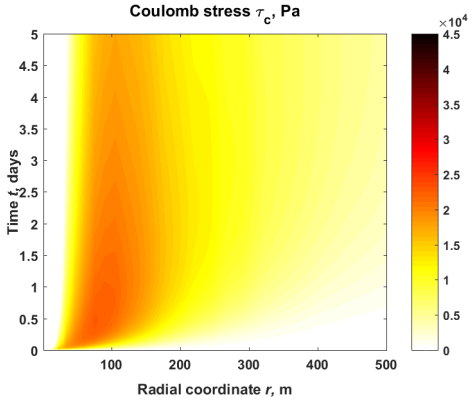

Figure G.11: Coulomb stress as a function of time and radial coordinate, $p_{\text{res},0} = 1.0 \cdot 10^7$

G.5 Geometry with displaced fault

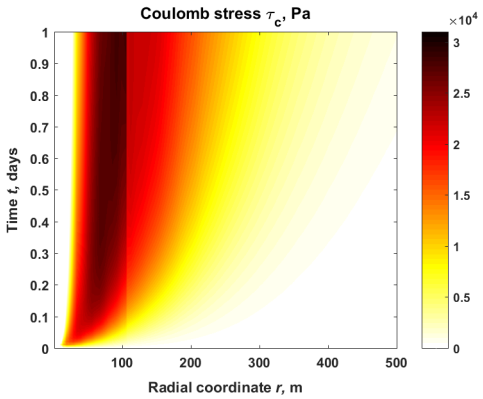

Figure G.12: Coulomb stress for a fault with a 5% throw relative to reservoir height, first day.

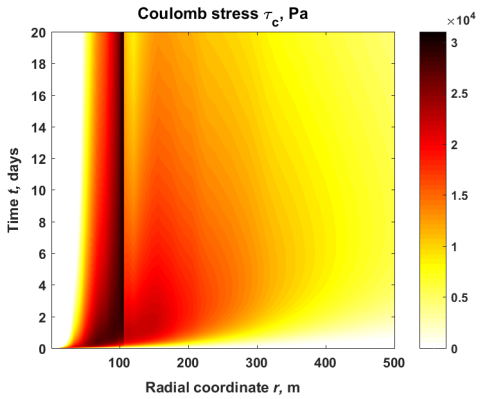

Figure G.13: Coulomb stress for a fault with a 5% throw relative to reservoir height, twenty days.

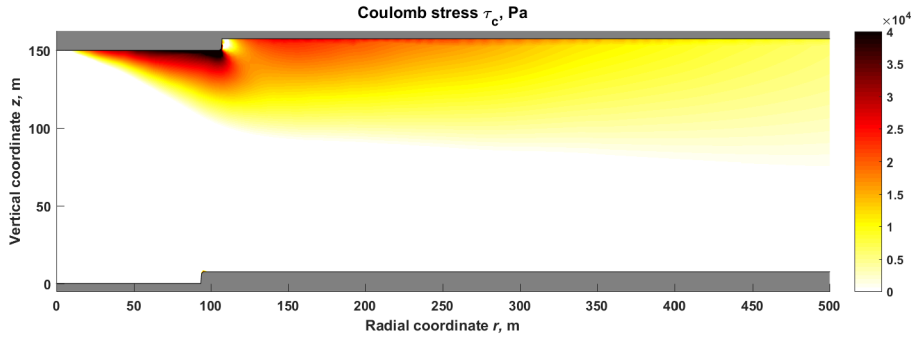

Figure G.14: *Coulomb stress for a fault with a 5% throw relative to reservoir height, t = 5 days.*

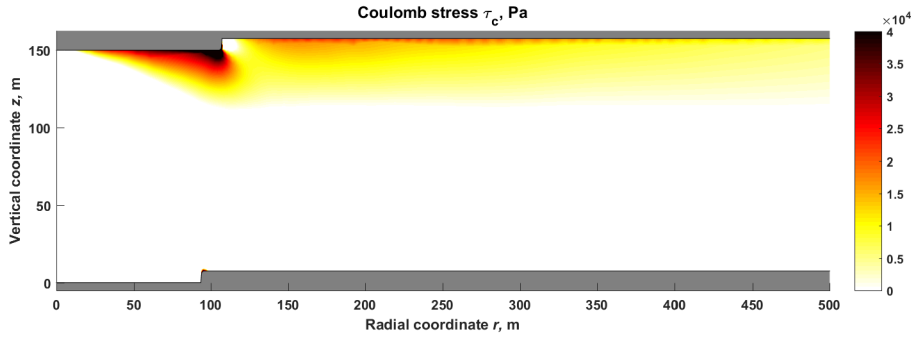

Figure G.15: *Coulomb stress for a fault with a 5% throw relative to reservoir height, t = 20 days.*

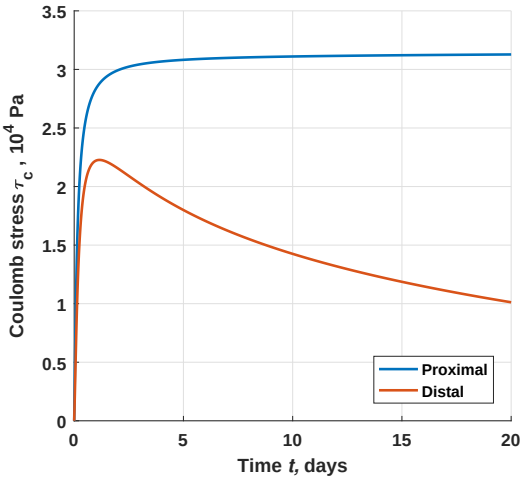

Figure G.16: Coulomb stresses versus time for the local maxima proximal and distal to the fault.

G.6 Geometry with displaced fault, uniform depletion

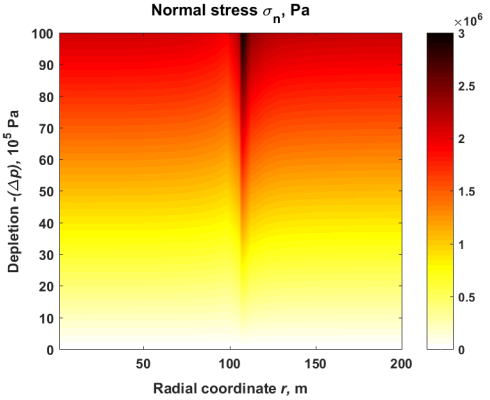

Figure G.17: Normal stress for a fault dipping towards the producer at $\theta = 85°$, uniform depletion.

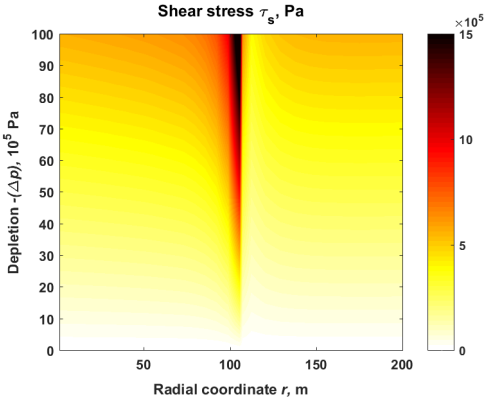

Figure G.18: Shear stress for a fault dipping towards the producer at $\theta = 85°$, uniform depletion.

H: Relative rate of earthquake production as predicted by rate-and-state friction model

H.1 Production rate

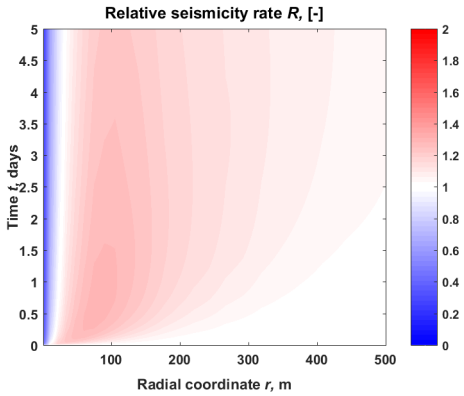

Figure H.1: Relative seismicity rate as a function of time and radial coordinate, $q_{sc} = 2.0 \cdot 10^6$ m^3/day.

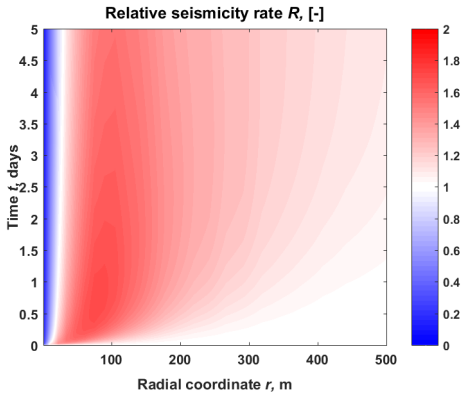

Figure H.2: Relative seismicity rate as a function of time and radial coordinate, $q_{sc} = 4.0 \cdot 10^6$ m^3/day.

H.2 Production ramping

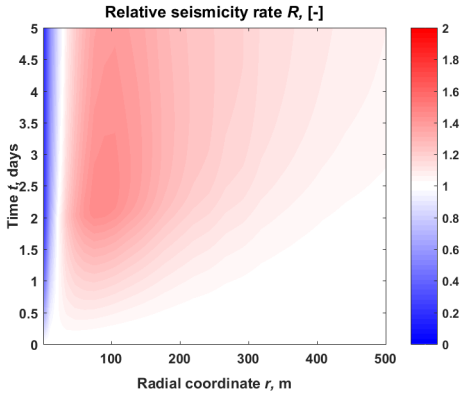

Figure H.3: Relative seismicity rate as a function of time and radial coordinate, $n_{\Delta q} \rightarrow \infty$.

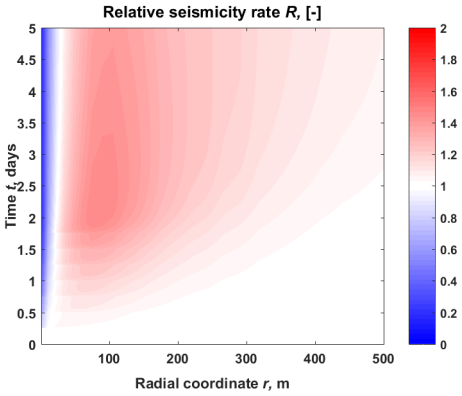

Figure H.4: Relative seismicity rate as a function of time and radial coordinate, $n_{\Delta q} = 7$.

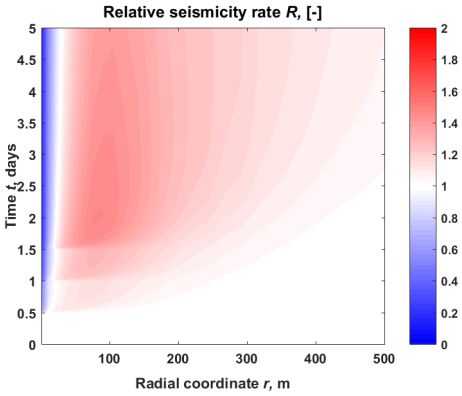

Figure H.5: Relative seismicity rate as a function of time and radial coordinate, $n_{\Delta q} = 3$

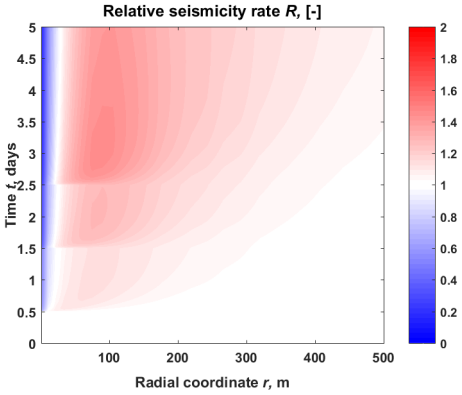

Figure H.6: Relative seismicity rate as a function of time and radial coordinate, $\Delta t = 2$.

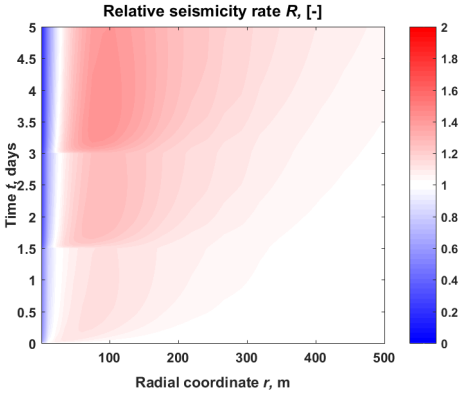

Figure H.7: Relative seismicity rate as a function of time and radial coordinate, $\Delta t = 3$

H.3 Reservoir pressure

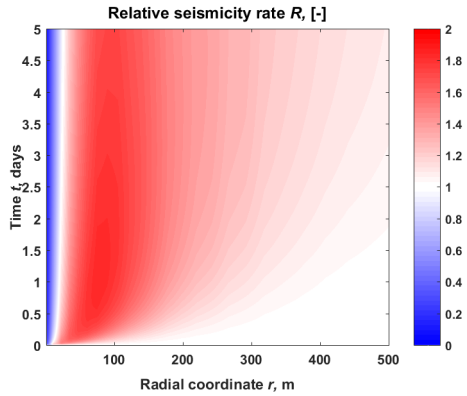

Figure H.8: Relative seismicity rate as a function of time and radial coordinate, $p_{\text{res},0} = 5.0 \cdot 10^6$.

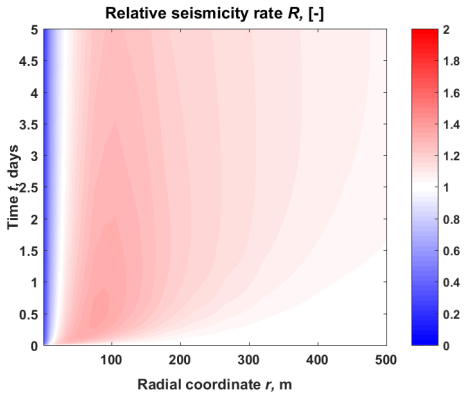

Figure H.9: Relative seismicity rate as a function of time and radial coordinate, $p_{\text{res},0} = 1.0 \cdot 10^7$

H.4 Geometry with displaced fault

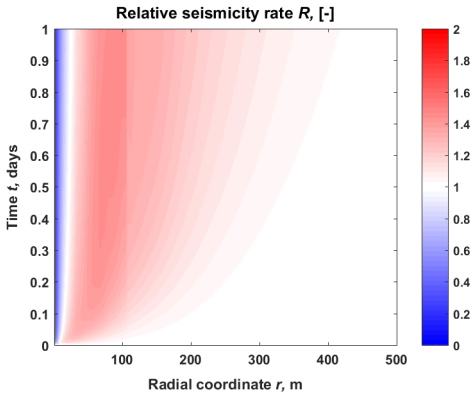

Figure H.10: Relative seismicity rate for a fault with a 5% throw relative to reservoir height, first day.

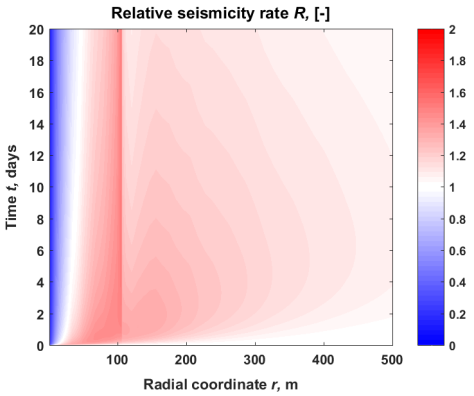

Figure H.11: Relative seismicity rate for a fault with a 5% throw relative to reservoir height, twenty days.

References

Al-Hussainy, R., H.J. Ramey, Jr and P.B. Crawford (1966). The flow of real gases through porous media. *Journal of Petroleum Technology*, 18 (5), 624-636.

Azizi, N., R. Behbahani and M.A. Isazadeh (2010). An efficient correlation for calculating compressibility factor of natural gases. *Journal of Natural Gas Chemistry*, 19, 642-645.

Baisch, S., R. Weidler, R. Vörös, D. Wyborn, and L. de Graaf (2006). Induced seismicity during the stimulation of a geothermal HFR reservoir in the Cooper Basin, Australia. *Bull. Seismol. Soc. Am.*, 96 (6), 2242-2256.

Bao, X. and D.W. Eaton (2016). Fault activation by hydraulic fracturing in western Canada. *Science*, 354 (6318), 1406-1409.

Bear, J. and M.Y. Corapcioglu (1981). Mathematical model for regional land subsidence due to pumping: 2. Integrated aquifer subsidence equations for vertical and horizontal displacements. *Water Resources Research*, 17 (4), 947-958.

Bourne, S. J., S. J. Oates, J. van Elk, D. Doornhof (2014). A seismological model for earthquakes induced by fluid extraction from a subsurface reservoir. *Journal of Geophysical Research: Solid Earth*, 119 (12), 8991-9015.

Carter, J.P. and J.R. Booker (1982). Elastic consolidation around a deep circular tunnel. *International Journal of Solids and Structures*, 18 (12), 1059-1074.

Carr, N.L., R. Kobayashi and D.B. Burrows (1954). Viscosity of hydrocarbon gases under pressure. *Journal of Petroleum Technology*, 6 (10), 47-55.

Cheng, A.H.D. (2016). *Poroelasticity*, Theory and applications of transport in porous media, vol. 27, Springer publishing.

Chessa, J. (2002). *Programming the finite element method with Matlab*, Northwestern University, Evanston, IL.

Cleary, M.P. (1977). Fundamental solutions for a fluid-saturated porous solid. *International Journal of Solids and Structures*, 13 (9), 785-806.

Clegg, M.W. (1967). Some approximate solutions of radial flow problems associated with production at constant well pressure. *Society of Petroleum Engineers Journal*, 7 (1), 32-41.

Deichmann, N. and D. Giardini (2009). Earthquakes induced by the stimulation of an enhanced geothermal system below Basel (Switzerland). *Seismological Research Letters*, 80, 784-798.

Dieterich, J. (1994). A constitutive law for rate of earthquake production and its application to earthquake clustering. *Journal of Geophysical Research*, 99, 2601-2618.

Ellsworth, W.L. (2013). Injection-induced earthquakes. *Science*, 341 (6142), 1225942.

Helm, D.C. (1994). Horizontal aquifer movement in a Theis-Thiem confined system. *Water Resources Research*, 30 (4), 953-964.

Holland, A. (2013). Earthquakes triggered by hydraulic fracturing in south-central Oklahoma. *Bulletin of the Seismological Society of America*, 103 (3), 1784-1792.

Hsieh, P.A. and R.L. Cooley (1995). Comment on 'Horizontal aquifer movement in a Theis-Thiem confined system' by Donald C. Helm. *Water resources research*, 31 (12), 3107-3111.

Jacob, C.E. (1940). On the flow of water in an elastic artesian aquifer. *Transactions of the American Geophysical Union*, 21 (2), 574-586.

Karimi-Fard, M., L.J. Durlofsky and K. Aziz (2003). An eficient discrete fracture model applicable for general purpose reservoir simulators. *Proceedings of the SPE Reservoir Simulation Symposium*, Houston, TX, 3-5 February 2003.

Lucas, K. (1981). Die Druckabhängigkeit der Viskosität von Flüssigkeiten - ene einfache Abschätzung. *Chemie Ingenieur Technik*, 53 (12), 959-960.

McGarr A., D. Simpson, L. Seeber (2002). Case histories of induced and triggered seismicity. In: Lee, W.K.H. et al. (eds.) *International Handbook of Earthquake and Engineering Seismology* 81A, 647-661, Academic Press, London.

Monfared, A.K. and L. Rothenburg (2015a). Poroelastic stress modifications surrounding a fully-penetrating injection well. *Journal of Petroleum Science and Engineering* 135, 660-670.

Monfared, K.A. and L. Rothenburg (2015b). A numerical study of poroelastic geomechanical processes during fluid injection in confined geological reservoirs. In *Proc. 15th Pan-American Conference on Soil Mechanics and Geotechnical Engineering (PCSMGE) / 8th South American Congress on Rock Mechanics (SCRM), 'From fundamentals to applications in geotechnics'*, Buenos Aires, 15-18 November, 1207-1214. IOP Press, Amsterdam.

Mukuhira, Y., C. Dinske, H. Asanuma, T. Ito, and M.O. Häring (2016). Pore pressure behavior at the shut-in phase and causality of large induced seismicity at Basel, Switzerland. *Journal of Geophysical Research: Solid Earth*, 121, 1-25.

Mulders, F.M.M. (2016). Modelling of stress development and fault slip in and around a producing gas reservoir. *PhD thesis, Delft University of Technology*.

Nederlandse Aardolie Maatschappij (2016). Winningsplan Groningen Gasveld *http://www.nam.nl/gas-en-oliewinning/groningen-gasveld/winningsplan-groningen-gasveld.html*.

Raleigh, C.B., J.H. Healy, and J.D. Bredehoeft (1976). An experiment in earthquake control at rangely, Colorado. *Science*, 191 (4233), 1230-1237.

Rudnicki, J.W. (1986). Fluid mass sources and point forces in linear elastic diffusive solids. *Mechanics of Materials* 5 (4), 383-393.

Segall, P. (1989). Earthquakes triggered by fluid extraction. *Geology* 17 (10), 942-946.

Segall, P. and S. Fitzgerald (1998). A note on induced stress changes in hydrocarbon and geothermal reservoirs. *Tectonophysics*, 289 (1-3), 117-128.

Segall, P. and S. Lu (2015). Injection-induced seismicity: poroelastic and earthquake nucleation effects. *Journal of Geophysical Research: Solid Earth*, 120, 5082-5103.

Shapiro, S.A., O.S. Krüger and C. Dinske (2013). Probability of inducing given-magnitude earthquakes by perturbing finite volumes of rocks. *Journal of Geophysical Research: Solid Earth* 118 (7), 3557-3575.

Shapiro, S.A. (2015). *Fluid-induced seismicity*. Cambridge University Press, Cambridge.

Shirzaei, M., W.L. Ellsworth, K.F. Tiampo, P.J. González, and M. Manga (2016). Surface uplift and time-dependent seismic hazard due to fluid injection in eastern Texas. *Science*, 353 (6306), 1416-1419.

Soltanzadeh, H. and C.D. Hawkes (2008). Semi-analytical models for stress change and fault reactivation induced by reservoir production and injection. *Journal of Petroleum Science and Engineering*, 60, 71-85.

Sternberg, Y.M. (1969). Some approximate solutions of radial flow problems. *Journal of Hydrology*, 7 (2), 158-166.

Theis, C.V. (1935). The relation between the lowering of the piezometric surface and rate and duration of a well using groundwater storage. *Transactions of the American Geophysical Union*, 16 (2), 519-524.

Van Everdingen, A.F. and W. Hurst (1949). The application of the Laplace transformation to flow problems in reservoirs. *Journal of Petroleum Technology*, 12 (1), 305-324.

Van Thienen-Visser, K. and J.N. Breunese (2015). Induced seismicity of the Groningen gas field: history and recent developments. *The Leading Edge*, June 2015.

Van Wees, J.D., L. Buijze, K. Van Thienen-Visser, M. Nepveu, B.B.T. Wassing, B. Orlic, and P.A. Fokker (2014). Geomechanics response and induced seismicity during gas field depletion in the Netherlands. *Geothermics*, 52, 206-219.

Verruijt, A. (2016). *Theory and problems of poroelasticity*, www.geo.verruijt.net.

Wang, H. (2000). *Theory of linear poroelasticity with applications to geomechanics and hydrogeology*, Princeton University Press.

Williams, M.L. (1952). Stress singularities resulting from various boundary conditions in angular corners of plates in extension. *International Journal of Solids and Structures*, 43 (17), 5100-5109.

Zbinden, D., A. Pio Renaldi, L. Urpi and S. Wiemer (2017). On the physics-based processes behind production-induced seismicity in natural gas fields. *Journal of Geophysical Research: Solid Earth*, 122 (5), 3792-3812.

Zoback, M.D. and S.M. Gorelick (2012). Earthquake triggering and large scale geologic storage of carbon dioxide. *Proceedings of the National Academy of Sciences USA*, 109, 10164-10168.